SHALE GAS WELL FRACTURE SURFACE AREA CALCULATION RE-VISITED FOR DYNAMIC FORMATION PERMEABILITY

A Thesis

by

LAURA PELAEZ SONI

Submitted to the Office of Graduate and Professional Studies of
Texas A&M University
in partial fulfillment of the requirements for the degree of

MASTER OF SCIENCE

Chair of Committee,	I. Yucel Akkutlu
Committee Members,	J. Bryan Maggard
	Yalchin Efendiev
Head of Department,	Dr. A. Daniel Hill

December 2016

Major Subject: Petroleum Engineering

ABSTRACT

Shale gas wells exhibit long-term transient linear flow, which is in most cases the only flow regime available for analysis in these wells. Several methods have been developed to analyze transient linear flow in shale gas wells by adjusting solutions for tight gas wells, assuming both homogeneous and dual-porosity reservoirs. These analytical models use the slope of the inverse of rate vs. square root of time plot to calculate reservoir parameters such as the flow parameter ($A\sqrt{k}$), fracture half-length (x_f) and total fracture surface area. However, the derivation of these methods neglects the stress dependent nature of formation permeability and the effects of molecular transport mechanisms on gas production.

In this work, a synthetic data simulation model was used to forecast gas production from a shale reservoir with dynamic matrix permeability. The production data was analyzed using conventional rate transient analysis (RTA) to calculate the value of total fracture surface area. Using a dynamic permeability model with mechanical effects, results show that the error in total fracture surface area caused by the assumption of constant permeability in the reservoir ranges from 9% to 28%. When molecular transport mechanisms are included in the dynamic permeability model, the range of the error in surface area becomes 1% to 323%. Sensitivity analysis shows that stress-dependent parameters, which affect matrix permeability in the area away from the fractures, have the highest impact on the surface area error.

A modified RTA model is presented in this work which accounts for dynamic permeability in the shale matrix by introducing pseudo-pressure and pseudo-time definitions. Results show that the model is able to retrieve the correct value of total fracture surface area from the production data. Since the calculation is independent of time, total fracture surface area can be calculated early in the life of the well to evaluate the effectiveness of the hydraulic fracturing job.

DEDICATION

To my beloved parents, Benigno and Laura, for their unconditional support and encouragement; making you proud is the greatest joy of my life. To my wonderful and smart sisters, Alejandra and Maria Jose, your accomplishments inspire me to become better and work harder. To my loving grandparents, for understanding that I had to go far away to accomplish my dreams. To the amazing and fun friends I made during my college and graduate career at Texas A&M; I will never forget all the memories we shared. Finally, and most importantly, thank you God for all the opportunities you have blessed me with, and for allowing me to finish my academic career successfully.

ACKNOWLEDGEMENTS

I would like to thank my committee chair, Dr. Akkutlu, for his support, patience and guidance during the course of this research. Your kind and uplifting words always encouraged me to move forward. I would like to thank Dr. Maggard, your help was invaluable in the most critical moments. Thanks for spending your time tutoring me and getting me unstuck. Also, thanks to Dr. Efendiev for serving on my committee; your input and feedback is very much appreciated.

Thanks to Baker Hughes for giving me a fellowship that helped me complete my studies. Thanks for believing in the capabilities of young, Latin females in the petroleum engineering department.

Thanks to the College of Engineering for giving me the opportunity and funding my semester abroad at Texas A&M Qatar. It was the best experience of my life.

Thanks also go to my friends and colleagues in the department, especially Prashant Sharma and Reza Ghasemi, who were patient, supportive and helped me complete my research. Finally, thanks to the faculty and staff for making my time at Texas A&M University a great experience.

NOMENCLATURE

A	=	Total fracture surface area [ft^2] or [acres]
$A\sqrt{k}$	=	Flow parameter [ft^2 $md^{1/2}$]
C_g	=	Gas compressibility [1/psia]
C_t	=	Total compressibility of the formation [1/psia]
D	=	Matrix pore diffusion coefficient [m^2/s]
D_D	=	Dimensionless drawdown [-]
D_s	=	Sorbed-phase diffusion coefficient [m^2/s]
F_{CD}	=	Dimensionless fracture conductivity [-]
f_{cp}	=	Slope correction factor [-]
h	=	Net formation thickness [ft]
k	=	Matrix permeability [md]
k_f	=	Fracture permeability [md]
k_{gas}	=	Apparent matrix permeability for gas flow [md]
k_{init}	=	Matrix stress-sensitive permeability at initial pressure [psia]
k_m	=	Matrix stress-sensitive permeability [md]
K_n	=	Knudsen number [-]
k_0	=	Matrix permeability at zero effective stress [md]
m	=	Parameter associated with the surface roughness of the pores, [-]

$m(p_i)$	=	Real gas pseudo-pressure at initial pressure [psia^2/cp]
$m(p_{wf})$	=	Real gas pseudo-pressure at flowing wellbore pressure [psia^2/cp]
$m(p)_k$	=	Real gas pseudo-pressure with dynamic permeability [md psia^2/cp]
m_{cp}	=	Slope of $1/q_g$ vs. $\sqrt{t}$ plot [D$^{1/2}$/Mscf]
m_{cp}	=	Slope of $1/q_g$ vs. $\sqrt{t_{ap}}$ plot [cp$^{1/2}$ D$^{1/2}$/Mscf md$^{1/2}$ psi$^{1/2}$]
n	=	Number of fractures [-]
p	=	Reservoir pore pressure [psia]
P_c	=	Confining pressure [psia]
p_L	=	Langmuir pressure [psia]
p_1	=	Effective stress at which pores are closed completely [psia]
q_D	=	Dimensionless flow rate [-]
q_g	=	Gas flow rate [Mscf/D]
T	=	Absolute temperature [R]
t_{ap}	=	Real gas pseudo-time [md psia D/cp]
$t_a(p)$	=	Agarwal's real gas pseudo-time [psia hours/cp]
t_D	=	Dimensionless time [-]
t_{Dxf}	=	Dimensionless time bases on x_f [-]
t_{Dye}	=	Dimensionless time based on y_e [-]

t_n	=	Normalized time [D]
V_s	=	Sorbed-phase amount [scf/ton]
V_{sL}	=	Langmuir volume [scf/ton]
w	=	Fracture width [ft]
x_e	=	Reservoir half-width [ft]
x_f	=	Fracture half-length [ft]
y_e	=	Distance from fracture to outer boundary [ft]

Greek Letters:

α	=	Biot's coefficient or effective stress coefficient [-]
ε_{ks}	=	Total organic grain volume per total grain volume [m^3/m^3]
λ	=	Mean free path of fluid molecules [m]
μ	=	Gas viscosity [cp]
ϕ	=	Porosity [fraction]

TABLE OF CONTENTS

Page

LIST OF FIGURES

Page

LIST OF TABLES

Page

CHAPTER I

INTRODUCTION

In petroleum engineering, many analytical solutions have been developed throughout the years to model fluid flow in porous media with the purpose of understanding how hydrocarbons in both, liquid and gas states, flow through the reservoir and into the wellbore. The end goal of these efforts is to be able to predict the amount of recoverable hydrocarbons, to plan the development of the field accordingly, and to make accurate economic assessments. The majority of analytical solutions have been developed for liquid flow in conventional reservoirs and then adapted to model gas flow. Nowadays, research is focused on modifying analytical solutions to be applied in unconventional reservoirs.

The interest in unconventional resources such as tight oil/gas, shale oil/gas and coal-bed methane has grown exponentially in recent years. The United States is the number one producer of resource shale in the world. Production from shale involves a complex system including a hydraulic fractured horizontal well, with a matrix that may or may not be naturally fractured and a very low permeability matrix beyond the fracture tips. Thus, analytical models developed for shales have to be derived integrating previous work in several areas: fluid flow in porous media, naturally fractured reservoirs, horizontal wells, hydraulic fracturing and tight reservoirs. Additionally, a deeper understanding of the petrophysics of shales, including the storage and transport mechanisms present, is key to improve the models and productivity from these reservoirs.

1.1 Introduction of the Shale Matrix

The shale matrix has a characteristic dual porosity system as seen in **Fig. 1,** that consists of organic round pores with size <10 nm and inorganic slit-shape pores that can be 100 nm or larger (Ambrose et al., 2012). The difference between the shape and size of the pores introduces a multi-scale feature that becomes important for fluid storage and transport. Gas is stored in the matrix as free fluid, adsorbed fluid and absorbed fluid. Free fluid refers to the conventional natural gas which storage is controlled by gas compressibility and the pore volume available for expansion. Gas is stored as free fluid in fractures, inorganic pores and the center of large organic nanopores. Adsorbed fluid refers to the gas that is attached to the internal pore walls, with large surface area. Hence, its storage is dependent on surface area available rather than pore volume. Gas stored in organic pores is mostly in adsorbed state, since the organic pore walls have large surfaces and a strong affinity to the hydrocarbon molecules. Absorbed fluid, refers to the gas that is dissolved in the organic solid. The term sorbed fluid is used in the literature and in this thesis, to refer to both adsorbed and absorbed states.

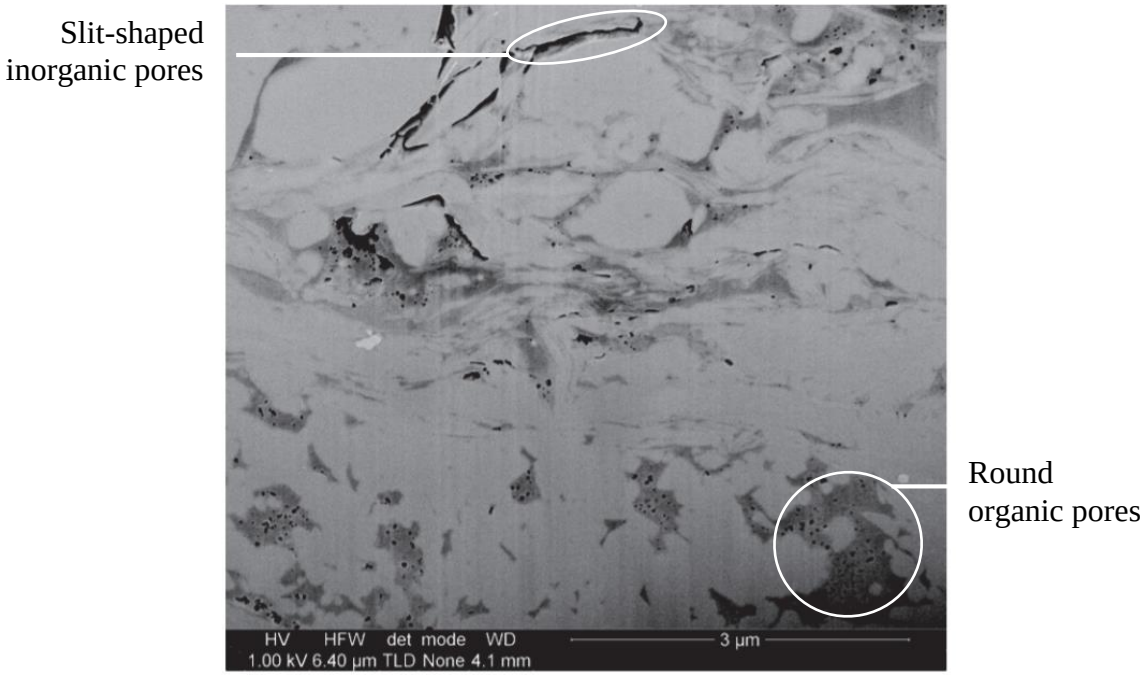

Figure 1 - FIB-SEM Image Showing the Dual Porosity of the Shale Matrix from Ambrose et al. (2012)

The discussion will now focus on flow regimes responsible for gas transport in shales. The Knudsen number is a dimensionless number that is used to classify different flow regimes for free gas defined as $K_n = \frac{\lambda}{H}$. In this equation, λ refers to the mean free path and H to the size of the capillary. Mean free path is a measure of the ratio between fluid-fluid molecular interactions to fluid-wall molecular interactions (Karniadakis et al., 2005). The analysis of K_n is usually centered around capillary size, or in this case, pore size. As the pore size decreases, the Knudsen number increases. In the shale matrix, inorganic slit-shaped pores have a pore size large enough so that flow is laminar and can be described by the classical continuum flow theory. In contrast, the size of the organic pores is much smaller, which may cause a significant increase in K_n depending on the

pressure. This means that there are less molecules in the pore, and thus it becomes difficult to treat the fluid as a continuum. Consequently, in these pores, flow changes from viscous to free-molecule flow, also known as Knudsen diffusion. However, there is research (Fathi et al., 2012) that shows that Kundsen diffusion most likely does not occur significantly in the organic pores since shales are over-pressured and produced at a bottom hole flowing pressure of 500 psi or higher. Nevertheless, since the pore size is small, there may be not enough molecules in the pore for a velocity profile to be developed for viscous flow. Thus, pore diffusion obeying Fickian diffusion can be used to describe this molecular flow (Wasaki, 2015).

In regards to the sorbed-phase, it has been shown that it can be mobile under the reservoir conditions (Fathi and Akkutlu (2009), Riewchotisakul (2015)). Thus, sorbed-phase transport obeys Fickian diffusion. Moreover, the sorbed phase amount (V_s) can be modeled using the Langmuir isotherm, shown in **Eq. 1.1**, which is a mono-layer adsorption model described by two parameters: Langmuir volume (V_{sL}) and Langmuir pressure (p_L) at any given pore pressure (p).

$$V_s = V_{sL}\frac{p}{p + p_L} \tag{1.1}$$

1.2 Introduction to Rate Transient Analysis

Shale gas wells have a characteristic high initial flowrate at the beginning of production which is due to the flow of gas in the hydraulic fractures. During this initial time, the contribution to production from the matrix is negligible. However, the production rate decreases rapidly and abruptly after this stage. These lower production rates are representative of the flow of gas from the matrix stimulated by the fractures. In rate transient analysis (RTA), this flow regime is called the matrix transient flow, and it is characterized by a negative half-slope in a log-log plot of gas flow rate versus time. Even though the production rates are significantly lower, formation linear flow usually accounts for the majority of the life of the well and thus the contribution of the gas flowing from the matrix becomes significant. Since the transition to matrix linear flow occurs early in the life of the shale gas wells, it is the only flow regime that can be analyzed. RTA is a commonly used method to analytically determine the value of some critical reservoir parameters such as permeability, the flow parameter ($A\sqrt{k}$), fracture half-length and fracture surface area. This production analysis is valuable since it is fast to perform, inexpensive and yields reliable results. However, in practice, flow rates of wells in tight/shale gas reservoirs can be over predicted using gas flow equations based on Darcy's law. Several authors (Vairogs et al. (1971), Heller and Zoback (2013), Kwon (2004)) have shown that these low flowrates are caused by a reduction in permeability due to effective stress exerted on the shale matrix. However, the analytical models available assume constant permeability.

1.3 Scope of the Work and Its Novelty

The main objective of this thesis is to re-visit the linear transient flow theory (Wattenbarger et al., 1998) and modify the RTA method to calculate total fracture surface area accounting for a stress-sensitive dynamic matrix permeability and molecular transport mechanisms acting on transport in the matrix. Additionally, a sensitivity analysis will be performed to determine if the effect on gas transport from pore and sorbed-phase diffusion is meaningful at field-scale.

The novelty of the proposed modified analytical model is that it accounts for stress-dependent permeability and molecular effects ignored by previous methods. The benefits include that uncertain parameters such as permeability and fracture half-length are not an input in the area equations; thus, these uncertainties do not hinder the accuracy of the total fracture surface area calculation. Moreover, the surface area calculation is independent of time. Thus, as long as the well exhibits formation linear flow, an accurate value for surface area can be calculated. This means that the surface area calculation can be performed early in the life of the well to evaluate the effectiveness of the hydraulic fracturing job.

CHAPTER II

LITERATURE REVIEW

This thesis proposes a modification to Wattenbarger et al. (1998) method to calculate matrix/fracture surface area by analyzing a shale gas well's long term transient linear flow. Several authors have discussed the reasons why long-term linear flow occurs in tight-gas and shale gas wells. Bello (2009) argues that in shale gas wells, linear flow occurs because of the flow of gas from the very-low permeability matrix to the highly permeable hydraulic fractures. Arevalo Villagran et al. (2001) showed that parallel natural fractures result in permeability anisotropy that causes long term linear flow.

2.1 Transient Linear Flow into Fractured Tight Gas Wells

The earlier literature focused on analyzing transient linear flow for tight gas wells. This became a reference and stepping stone for the similar analysis of shale gas wells, since both have characteristically very low permeability. Wattenbarger et al. (1998) developed a method to calculate $\sqrt{k}\, x_f$ and drainage area based on the analysis of the square root of time plot for fractured tight gas wells in transient linear flow. The analysis uses the slope of this plot in addition to reservoir properties to calculate drainage area. This calculation of drainage area is practical since it does not require the value of permeability to be known, which is usually highly uncertain. Equations for constant pressure and constant rate inner boundaries are presented for linear flow in a rectangular reservoir. The detailed derivation of the equations proposed by Wattenbarger et al. (1998)

is presented in **Appendix A**. This method is the basis of the derivation of the modified model presented in this thesis to calculate total fracture surface area of a shale gas well.

Ibrahim and Wattenbarger (2005) realized that analytical solutions may significantly be in error when applied to transient linear flow instead of transient radial flow. The slope of the square root of time plot differs from the analytical solution as the flow rates, or degree of drawdown becomes higher. Thus, a correction factor is presented to correct the slope of the plot for a constant pressure case and improve the accuracy of the $A_c\sqrt{k}$ calculation. Since shale gas wells are commonly produced at high drawdown, this correction factor will be applied in the modified method proposed in this thesis.

Nobakht and Clarkson (2011) argued that using the slope of the square root time plot results in an overestimation of the target reservoir parameters. They claimed that the overestimation is dependent not only on the level of drawdown but also on formation compressibility. Thus, they developed a method that accounts for these factors and corrects the error in the slope. They explain that the overestimation occurs because the basis of the equations to calculate linear flow parameters is liquid flow theory and that introducing pseudo-pressure is not enough to account for gas flow. Thus in their method they introduce pseudo-time (Anderson and Mattar, 2007), which requires an average pressure in the region of influence. The authors argue that this method should be preferred over Ibrahim and Wattenbarger's correction factor since it is developed analytically rather than empirically and includes a correction for compressibility. A detailed discussion on pseudo-time will be presented at the beginning of Chapter 5.

2.2 Analytical Solutions for Transient Flow in Linear Reservoirs with Dual Porosity

Shale reservoirs have a characteristic dual porosity system, composed of very low permeability matrix blocks which store the fluid and high permeability fractures which carry the fluid to the well. Thus, shales can be described by the dual porosity model introduced by Warren and Root (1963). Warren and Root (1963) presented a method to analyze build-up data in double porosity reservoirs for slightly compressible fluids. Kucuk and Sawyer (1980) extended the analytical well testing methods to analyze reservoir parameters in Devonian gas shales, which can be used with pressure-squared or pseudo-pressure definitions. They include a brief discussion on the Klinkenberg effect and desorption in the shale matrix. They conclude that dual porosity reservoirs with a dimensionless time larger than 50, behave like a homogenous reservoir. El Banbi (1998) was the first author to present analytical solutions for transient flow in linear reservoirs with dual porosity. Bello and Wattenbarger (2010) extended El Banbi's solutions (1998) by modeling the hydraulically fractured shale gas well as a horizontal well draining a rectangular reservoir containing a fracture network connecting matrix blocks. In their work, Bello and Wattenbarger (2010) identified five flow regions for a multi-stage hydraulically fractured horizontal shale gas well. Production data exhibits region 4, which is transient linear flow, and this is the only region available for analysis in most wells. The equations to obtain dimensionless rate and $A_{cw}\sqrt{k}_f$ are derived in Laplace space for each flow region. In this case, the equation for region 4 can be used to determine the cross-sectional drainage area only if the permeability value, and other reservoir parameters are known.

This model was modified to account for radial flow towards an actual horizontal well using a "convergence skin" (Bello and Wattenbarger, 2010), which appears as a line with a significant intercept in the square root of time plot, instead of passing through the origin. This "skin effect" masks linear flow at early times. Thus, to correct for this "skin effect", the early behavior is modeled through the skin convergence factor to fit the curves on both the log-log $\frac{1}{q}$ plot and square root of time plot. Bello and Wattenbarger (2010) treated the "skin effect" as constant and developed an equation to include this skin effect in the analytical solution. This equation is only valid for transient (infinite acting) linear flow.

Ahmadi, Almarzooq and Wattenbarger (2010) extended the analytical dual porosity solution to include boundary dominated flow. Boundary dominated flow begins when the pressure at the center of the matrix block starts to decline. The mathematical model that the authors presented can be used to calculate drainage volume, and the area of interfaces between hydraulic fractures and the matrix and matrix permeability, in some cases. The authors showed that their method should be used in a well's earlier life rather than later life and that factors such as liquid loading, well interference and complex fracture patterns cannot be accurately analyzed by their method. However, gas adsorption is not taken into account in this method since the authors believed that during the transient flow regime, gas desorption effects are negligible.

2.3 Application of Linear Flow Analysis to Shale Gas Wells

Since the beginning of this decade, research focused on how to apply transient linear flow theory to shale gas wells in a simplified yet rigorous manner. Even though, as discussed in section 2.2, several authors developed analytical solutions based on the dual porosity nature of shale reservoirs, other researchers focused on adapting the solutions for the simpler single- porosity case to analyze production from shale gas reservoirs.

Nobakht et al. (2010) developed a method of production forecasting for tight/shale gas reservoirs that accounts for long-term transient linear flow and then shifts to hyperbolic decline when boundary-dominated flow begins. The advantage of this method is that it does not require any input values for permeability or fracture half-length, which are highly uncertain parameters. However, the value of drainage area must be specified. According to the authors, the need of introducing pseudo-time is avoided by using a hyperbolic decline based on the end of linear flow time. They argue that even though this technique may not accurately predict the result, the errors have no economic consequence since they occur at a very late time.

Wattenbarger's method which is the basis of transient linear flow theory assumes a bounded rectangular reservoir with a single fully-penetrating fractured well. However, shale reservoirs are produced by drilling multi-staged fractured horizontal wells and Anderson et al. (2010) believe that the single fracture model cannot represent the complexity of a multi-fractured horizontal well. Thus, they developed a method that includes a Stimulated Reservoir Volume (SRV) contained within an infinite-acting reservoir. They propose an analytical model that includes transient flow from the

stimulated matrix, followed by boundary-dominated flow as the boundary is seen, and then a return to matrix linear flow from the unstimulated matrix, which lies beyond the stimulated region by the hydraulic fractures. This shows that, if the matrix permeability is in the range of $1e^{-4}\,md$ or greater, the contribution of the unstimulated matrix is noticeable after two years. However, if the matrix permeability is $1e^{-6}\,md$, the contribution is negligible. This means that the contribution of the matrix is highly dependent on the assumed matrix permeability value, and this is a very uncertain parameter. However, there are other authors that oppose this position and show that in low permeability reservoirs, such as shales, the fractures define the lateral boundaries of the reservoir and that gas flow from the matrix beyond the fracture-tips is insignificant (Carlson and Mercer (1989), Mayerhofer et al. (2006)). The method proposed in this thesis is based on the latter position, which considers contribution from the unstimulated matrix negligible. Thus, the analytical model, which will be described in Chapter 3, assumes fractures that extend laterally until they reach the boundary.

Most of the analytical solutions developed for transient linear flow assume a constant pressure or constant rate inner boundary condition. For shale gas well analysis, a constant pressure assumption is usually preferred since the wells are produced at a large drawdown in order to maximize production rate. However, in reality it is very difficult to maintain a true constant rate or constant pressure in the well. Thus, Liang, Mattar and Moghadam (2011) proposed an approach to analyze transient linear flow with variable rate and pressure data. To analyze this scenario, they use material balance time as the superposition in time function. However, when using superposition in time (time is

shuffled back and forth), it is difficult to identify outliers in the data and this can lead to erroneous flow regime identification.

All of the methods presented in this section have assumed that the effects of gas desorption in the matrix have a negligible contribution to gas production. However, as explained in Chapter 1, there has been recent research that suggests that desorption and other molecular mechanisms can influence cumulative production of a shale gas well. In 2012, Xu et al. developed a method to analyze linear flow of a shale gas well that considered three flow regimes: bilinear flow, transient matrix linear flow and boundary-dominated flow. They included an investigation on the effect of adsorption isotherms and concluded that early in the life of the well, desorption had a negligible impact on production, but that its contribution was important for long-term production forecasting.
In this thesis, the author is challenging the notion of negligible molecular effects. Wasaki and Akkutlu (2015) showed that the molecular effects can enhance gas transport near the fracture. They suggested that the design of horizontal wells with multiple fracture stages should account for the geomechanical and diffusional effects on gas transport. Thus, the modified model proposed in this thesis to analyze matrix linear flow of a shale gas well accounts for a dynamic matrix permeability, and molecular effects such as desorption and pore and sorbed-phase diffusion in order to investigate the impact of the different transport mechanisms in field scale analysis.

CHAPTER III

TOTAL FRACTURE SURFACE AREA MODEL

3.1 Description of Simulation Model

The mathematical model used to derive the formula to calculate total fracture surface area follows the transient linear flow theory originally presented by Wattenbarger et al. (1998). A schematic of Wattenbarger's model is shown in **Fig. 2**. The features and assumptions used in this work are described below.

- The well is in the center of a closed rectangular drainage geometry.
- Infinite conductivity fractures extending all the way to the lateral drainage boundary($x_f = x_e$). The infinite conductivity assumption is valid for large dimensionless fracture conductivity, $F_{CD} > 50$. F_{CD} is a dimensionless parameter that relates fracture permeability (k_f), matrix permeability(k), fracture width (w), and fracture half-length (x_f) as shown in **Eq. 3.1**. (Wattengarger et al., 1998). It has been shown that the fractures define the boundaries of the reservoir and that the production contribution of the matrix beyond the stimulated region is negligible (Carlson and Mercer, 1989, Mayerhofer et al, 2006).

$$F_{CD} = \frac{k_f w}{k x_f} \tag{3.1}$$

- Homogeneous porosity system.
- The flow is linear from the matrix to the fractures.

Wattenbarger's method was developed for a model with a single- fracture vertical well. However, it is well known that shale gas reservoirs are produced with horizontal

multi-fractured wells assuming that the fractures do not interfere with each other. Nobakht et al. (2010) explained that even though the theory of transient linear flow was developed for a single fractured vertical well, it can also be applied to multi-fractured horizontal wells. Assuming that the fractures are equally spaced and that the well contributes relatively a small quantity of gas compared to the fractures, both systems would yield the same production rates. The reason is that there exist no-flow boundaries in between adjacent fractures during linear flow.

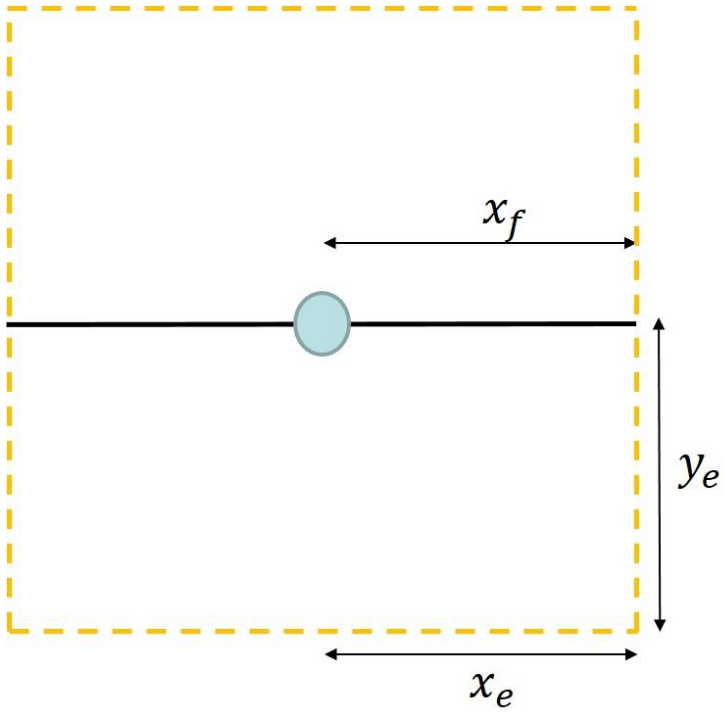

Figure 2 - Schematic of a Hydraulically Fractured Well in a Rectangular Reservoir

3.2 Development of the Analysis Equations

The detailed mathematical derivation of Wattenbarger's model is given in **Appendix A**. The original model is used to calculate drainage area and original gas in place (OGIP). However, this thesis focuses on calculating total fracture surface area, thus, it is necessary to highlight important parts of the derivation that lead to this calculation.

The analytical solution for linear flow in a rectangular reservoir with an inner constant pressure boundary condition, and an outer no-flow boundary condition is presented below (**Eq. 3.2**). This solution includes both transient and boundary-dominated flow regimes.

$$\frac{1}{q_D} = \frac{\frac{\pi}{4}\left(\frac{y_e}{x_f}\right)}{\sum_{n=1\ odd}^{\infty} \exp\left[-n^2 \frac{\pi^2}{4}\left(\frac{x_f^2}{y_e^2}\right) t_{Dxf}\right]} \tag{3.2}$$

This solution has a high level of complexity; thus a "short" term approximation can be made to describe only transient flow by assuming an infinite-acting reservoir shown in **Eq. 3.3**.

$$\frac{1}{q_D} = \frac{\pi}{2}\sqrt{\pi t_{Dxf}} \tag{3.3}$$

These analytical solutions for linear flow into a fracture were developed for slightly compressible fluids. Thus, in order to use for gas flow, they have to be adapted by using the real gas pseudo-pressure (Al-Hussainy, Ramey and Crawford, 1966). The following definitions for dimensionless rate (**Eq. 3.4**) and dimensionless time (**Eq. 3.5**) are used when analyzing gas wells. The difference between t_{Dye} and t_{Dxf} is that the

reference for the former is the distance to the reservoir boundary, and the fracture half-length distance is the reference for the latter.

$$\frac{1}{q_D} = \frac{kh\left[m(p_i) - m\left(p_{wf}\right)\right]}{1424\, q_g T} \tag{3.4}$$

$$t_{Dye} = \frac{0.00633kt}{(\phi\mu c_t)_i\, y_e^2} = t_{Dxf}\frac{x_f^2}{y_e^2} \tag{3.5}$$

where q_g is gas flow rate in Mscf/day, k is formation permeability in md, h is formation thickness in ft., T is absolute reservoir temperature in Rankin, t is time in days, ϕ is porosity, μ is viscosity in cp, C_t is total compressibility in psi^{-1}, x_f is fracture half-length in ft., y_e is distance to the lateral boundary in ft., and $m(p)$ is the real gas pseudo-pressure with units of psi^2/cp and defined by **Eq. 3.6**:

$$m(p) = 2\int_{p_0}^{p} \frac{p}{z\mu}\, dp \tag{3.6}$$

Substituting the definition of dimensionless rate in the "short term" approximation of the constant pressure solution (Eq. 3.3), the resulting equation (**Eq. 3.7**) can be manipulated to give a y = mx type linear equation as shown below.

$$\frac{1}{q_g} = \frac{315.4T}{h\sqrt{(\phi\mu c_t)_i}}\frac{1}{\Delta m(p)\sqrt{k}\, x_f}\sqrt{t} \tag{3.7}$$

This equation (3.7) is the basis of the square root of time plot ($\sqrt{t}$). The slope of this plot becomes an essential parameter to analyze transient linear flow. Since the production data will yield a value of the slope of the $\sqrt{t}$ plot, this value will be known (**Eq. 3.8**). Thus, it is more helpful to re-arrange the m_{cp} equation to solve for x_f (**Eq. 3.9**).

$$m_{cp} = \frac{315.4T}{h\sqrt{(\phi\mu c_t)_i}} \frac{1}{\Delta m(p)\sqrt{k}\, x_f} \tag{3.8}$$

$$x_f = \frac{315.4T}{h\sqrt{(\phi\mu c_t)_i}} \frac{1}{\Delta m(p)\sqrt{k}\, m_{cp}} \tag{3.9}$$

The units of the slope are $(1/D^{\frac{1}{2}}/Mscf)$. k is formation permeability in md, h is formation thickness in ft., T is absolute reservoir temperature in Rankin, ϕ is porosity, μ is viscosity in cp, C_t is total compressibility in psi^{-1}, x_f is fracture half-length in ft., and $\Delta m(p)$ is the real gas pseudo-pressure difference $(m(p_i) - m(p_{wf}))$ with units of psi^2/cp.

As introduced in the previous chapter, Ibrahim and Wattenbarger (2005) showed that the slope of the $\sqrt{t}$ plot differs from the analytical solution as the degree of drawdown becomes higher. Thus, the slope of the $\sqrt{t}$ plot has to be corrected using the following equations for drawdown (**Eq. 3.10**) and correction factor (**Eq. 3.11**), which are dimensionless quantities.

$$D_D = \frac{\left[m(p_i) - m\left(p_{wf}\right)\right]}{m(p_i)} \tag{3.10}$$

$$f_{cp} = 1 - 0.0852D_D - 0.0857D_D^2 \tag{3.11}$$

The target reservoir parameter of this thesis is total fracture surface area. In other words, it is the total area that is draining fluid into the fracture system. This is a critical parameter to evaluate production performance from the fractures. Based on the geometry of the model, total fracture surface area, in ft^2, can be calculated using **Eq. 3.12**.

$$A = 4hx_f n \tag{3.12}$$

where n is the number of fractures, h is the thickness of the formation in ft., and x_f is the fracture half-length which comes from Eq. 3.9 in ft. Thus, the final form of the equation after substituting the definition of x_f and multiplying by the correction factor is shown below (**Eq. 3.13**).

$$A = f_{cp} \frac{1261.2 \times T}{\sqrt{(\phi \mu C_t)_i}} \times \frac{1}{m_{cp} \times \sqrt{k} \times \Delta m(p)} \times n \tag{3.13}$$

3.3 Validation of the Model

In order to conduct the analysis on the value of total fracture surface area, a simulation model using synthetic data was created using the numerical simulator CMG/IMEX version 2015.10.1. First, the accuracy of the simulation model had to be verified and thus, the results of the simulation were compared to Wattenbarger's analytical solution for a fractured well in the middle of a rectangular reservoir previously shown in Eq. 3.3.

The task is to determine the constant pressure response of a fully penetrating horizontal well. A simple 3-D single-phase gas flow model was created using Builder version 2015.10.1. The simulation model includes a horizontal well with four fractures uniformly distributed in a rectangular reservoir as shown in **Fig. 3**. The reservoir is homogeneous and the fractures were simulated by using local grid refinement and increasing the permeability of the grid representing the fracture to 1000 md, making the assumption of infinite conductivity valid. The hydraulic fractures have a fracture half-length (x_f) of 312.5 ft. and fracture spacing of 200 ft. Thus, the distance from the fracture

to the boundary (y_e) is 100 ft., since there is a "no-flow boundary" effect at the middle of two fractures as shown in Fig. 3. The thickness of the fracture (h) is equal to the net thickness of the formation. The initial reservoir pressure is 3800 psi. The well is produced for one year with a constant bottom-hole pressure constraint of 500 psi. The summary of the reservoir parameter values that were used in the simulation model is shown in **Table 1**. The simulation is for a homogeneous reservoir with gas production only, in accordance to the assumptions of the analytical model.

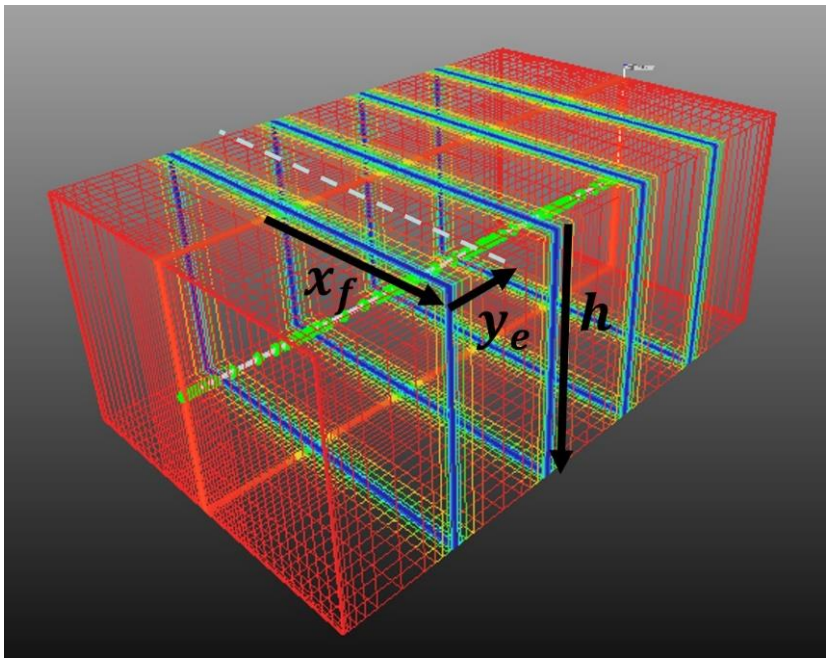

Figure 3 - Geometry of the Simulation Model Including a Horizontal Well with 4 Fracture Stages

Table 1 - Dataset for Simulation Model Validation

Reservoir properties		
Parameter	Value	Units
Initial reservoir pressure (p_i)	3800	*psi*
Constant bottom-hole pressure (p_{wf})	500	*psi*
Constant permeability value (k)	0.000005	*md*
Thickness (h)	415	*ft*
Temperature (T)	640	*R*
Porosity (φ)	0.06	-
Viscosity (μ)	0.0215	*cp*
Total compressibility (C_t)	2.30E-04	psi^{-1}
Fracture half-length (x_f)	312.5	*ft*
Distance to the boundary (y_e)	100	*ft*
Number of fractures (n)	4	-

The first step to validate the simulation model is to convert the gas rate results into dimensionless variables using Eq. 3.4 and Eq. 3.5. Then, the results from performing this simulation for a period of one year are checked against the analytical solution for the infinite-acting outer boundary case presented by Wattenbarger et al. (Eq. 3.3), since the well remains in transient linear flow during this period. It is important to remember to use the drawdown correction factor to adjust the analytical solution as shown in **Eq. 3.14**.

$$\frac{1}{q_D} = f_{cp}\frac{\pi}{2}\sqrt{\pi t_{Dxf}} \tag{3.14}$$

The results of this comparison are given in **Fig. 4** and they show a very good agreement between the analytical method and the results obtained from the simulation model. At early time, there is a slight difference, which can be attributed to fracture linear or bilinear flow or a skin factor that "masks" transient linear flow at early time. However, a perfect match occurs starting from $t_D = 1e^{-4}$, which is a very early time, so the results of the simulation model are concluded to be satisfactory. The next step is to verify that the equation developed for total fracture surface area (Eq. 3.13) is able to retrieve the surface area used in the simulation model. **Table 2** shows the value of total fracture surface area from both methods and the results differ by 1%. Thus, the validity of the equation is demonstrated.

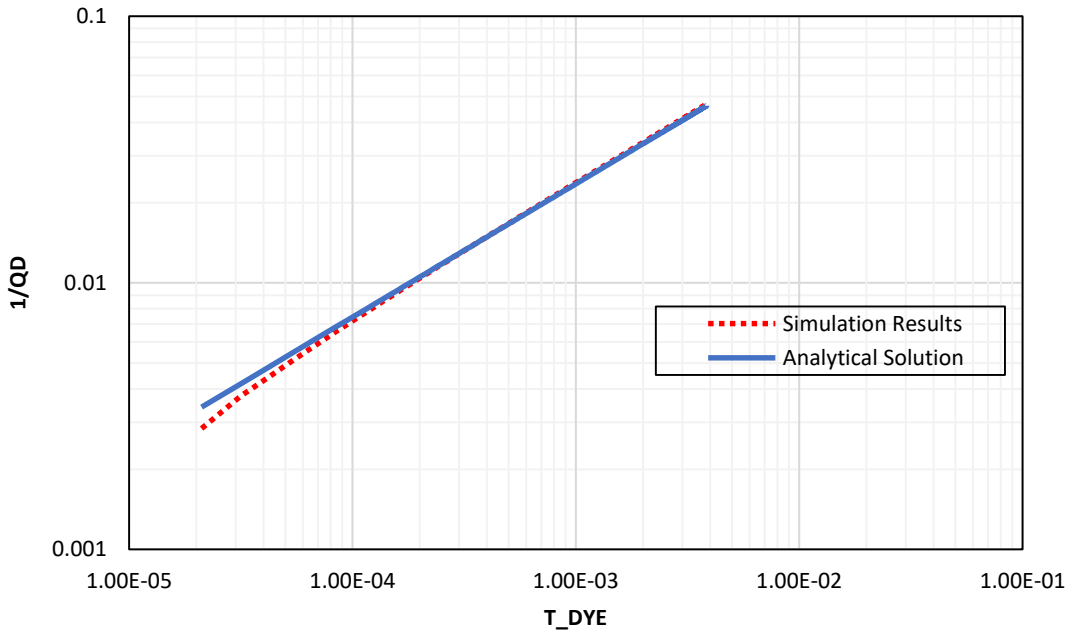

Figure 4 - Verification of the Simulation Model for a Horizontal Well in a Rectangular Reservoir

Table 2 - Total Fracture Surface Area Comparison Between Analytic and Simulation Models

Surface Area Calculation		
Simulation Model		
$A = 4 \times h \times x_f \times n$	2,075,000 47.64	*ft2* *acres*
Analytical Model		
$A = f_{cp} \times \frac{1261.2 \times T}{\sqrt{(\phi\mu C_t)_i}} \times \frac{1}{m_{cp} \times \sqrt{k} \times \Delta m(p)} \times n$	2,054,204 47.16	*ft2* *acres*
Error	-1.00	*%*

CHAPTER IV

IMPACT OF CONSTANT PERMEABILITY ASSUMPTION IN TOTAL SURFACE AREA CALCULATION

4.1 Discussion of Constant Permeability Assumption

For liquid flow, isothermal conditions, small and constant compressibility, constant viscosity and constant permeability can be assumed when deriving the diffusivity equation. This assumption makes the diffusivity equation linear. In contrast, for gas flow, it is well known that fluid compressibility and viscosity are dependent on pressure. These variations are accounted for by introducing the pseudo-pressure transformation. However, permeability is commonly assumed constant for the analytical application. The assumption of a pressure-independent permeability is acceptable for a variety of reservoirs where local pressure and permeability changes are small. However, this is not the case for gas transport in shales, where there are large pressure drops encountered as the gas flows through the matrix.

There is extensive research conducted on the stress-dependent fracture permeability because they are the main source of flow capacity in shales (Fredd et al. (2001); Wen et al. (2007); Zhang et al. (2014)). Similar to the aperture of the fractures decreasing as effective stress increases, the inorganic slit-shaped pores in the matrix are also being affected by the in-situ stresses (Heller and Zoback, 2013). Thus, the focus of this section is on the stress-sensitive nature of the matrix permeability in shales, which

differs from the traditional assumption of constant permeability widely used for conventional reservoirs.

Several authors (Vairogs et al. (1971), Heller and Zoback (2013), Kwon (2004)) have shown experimentally that the formation permeability in shales is stress-dependent. As gas is produced, the pore pressure decreases, which in turn causes an increase in effective stress on the rock, which results in compaction. The rock compaction causes the pore diameter to decrease, or even close and thus leading to a significant reduction in permeability. Vairogs et al. (1971) concluded that there is a greater degree of permeability reduction in low-permeability cores than in high-permeability cores. The reason behind this phenomenon is that tight cores have very small pore sizes and thus, the compressive stress applied reduce the flow capacity of these small pores proportionately more than that of larger pores. The pore shape is also a factor; the stress applied onto slit-shaped pores is not evenly distributed as it is for round-shape pores, making the slit-shaped pores more sensitive to stress.

Kwon (2004) showed that Gangi's model (1978) can be used to represent the stress-dependency of shales, which can be described as a matrix pore-network with slit-shaped pores. In the next section, Gangi's model will be used to describe the pressure-dependent formation permeability in order to determine if assuming a constant permeability in the analysis of a shale gas well, leads to an error in the total fracture surface area calculation or not.

4.2 Gangi's Stress-dependent Permeability Model

A constant permeability assumption has been determined to be invalid for describing gas flow in shales. This section will present Gangi's model, which can be used to model stress-dependent formation permeability. The permeability change of a fractured rock with confining pressure is calculated by a "bed of nails" model for the asperities of the fracture, or in this case, the slit-shaped pore, according to **Eq. 4.1**. A schematic model of Gangi's "bed of nails" is shown in **Fig. 5**.

$$k_m = k_0 \left[1 - \left(\frac{P_c - \alpha p}{P_1}\right)^m\right]^3 \tag{4.1}$$

k_0 is the permeability at zero effective stress, $P_c - \alpha p$ is the effective stress exerted on the matrix, α is the Biot's coefficient, also called the effective stress coefficient, p is the reservoir pore pressure, p_1 is the effective modulus of the asperities, which means the effective stress at which the pores are closed completely, and *m* is a factor associated with the surface roughness of the pores with values ranging from 0 to 1.

There are several assumptions for this model: 1) the slit-shaped pore is a very small crack and thus the flow is slow and laminar, 2) surface roughness of the crack does not have a big effect on the laminar flow, 3) the surface of the crack is smooth (angles <10°), and 4) the two surfaces of the crack are not a perfect match when they come in contact with each other because asperities keep them apart.

The challenge is to determine the variation of the aperture of the crack as the reservoir pore pressure (p) is reduced due to gas production. This depends on the shape of the asperities and the number in contact with each surface of the crack. The chosen shape

is rod-shape asperities because it is the simplest model and the distributions of the other shapes are equivalent to distributions using a rod-shape. A smooth surface would have a value of *m* very close to 1, as the height of the asperities is close to uniform, with very few short asperities. In contrast, a value of *m* close to zero means that the surface is rough with a significant variation in asperities' height.

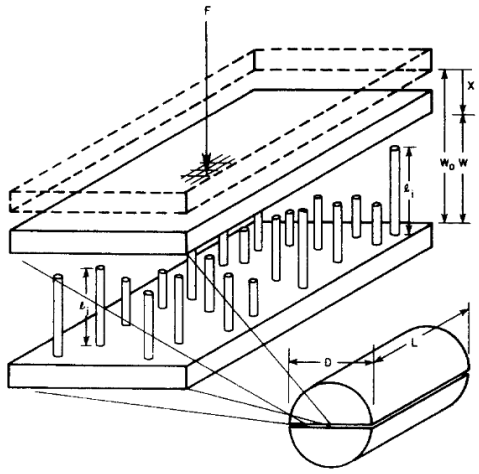

Figure 5 - Schematic Model of Gangi's "Bed of Nails" from Gangi (1978)

A dynamic formation permeability based on Gangi's model was introduced into the simulation model described in Chapter 3. **Table 3** shows the pressure-dependent input used in the simulation model. The shaded rows correspond to initial reservoir pressure and constant bottom-hole flowing pressure.

Table 3 - Dynamic Reservoir Data based on Gangi's Model used in Forward Simulation

Pressure	*Z-factor*	*Viscosity (cp)*	*km (md)*
500	0.963733915	0.013669201	3.00659E-06
700	0.950860317	0.013941863	3.10103E-06
900	0.939122689	0.014253261	3.19777E-06
1000	0.933722206	0.014422801	3.247E-06
1100	0.928655711	0.01460129	3.29683E-06
1300	0.919585331	0.01498432	3.39828E-06
1500	0.912021194	0.015400666	3.50215E-06
1700	0.906049181	0.015848335	3.60849E-06
1900	0.90172527	0.016324923	3.71735E-06
2100	0.89907184	0.016827618	3.82878E-06
2300	0.898077125	0.017353283	3.94283E-06
2500	0.898697843	0.017898574	4.05954E-06
2700	0.900864355	0.018460085	4.17897E-06
2900	0.904487312	0.01903448	4.30117E-06
3100	0.909464623	0.019618594	4.4262E-06
3500	0.92304755	0.020804631	4.68494E-06
3800	0.935986056	0.021700204	4.88683E-06

4.2.1 Importance of the Constant Permeability Value Selection in the Analytical Model

The objective of this section is to determine the consequence of assuming a constant permeability when analyzing the production of a gas well from a reservoir with dynamic permeability. In other words, the simulation model with dynamic permeability based on Gangi's model will be analyzed using Wattenbarger's method (1998), as described in Chapter 3, which is derived based on the constant permeability assumption.

Wattenbarger's method (1998) requires a constant permeability value input to calculate total fracture surface area. Thus, the following question arises: what value of permeability should be used in the analytical model? In this thesis, two different options for constant permeability value will be investigated. The first option is to use a permeability measurement with a sample under zero effective-stress; in Gangi's model,

this permeability value is defined as k_0. A reasonable value for k_0 could be obtained using extrapolation on the k_m vs. stress plot. Alternatively, one would consider using transient data from helium expansion porosimetry under pressures above 500 psi. k_0, however, is not equivalent to the stress-free crushed particle measurements. **Table 4** shows Gangi's model parameters that were used in the simulation model and **Table 5** shows the reservoir parameters used in the rate transient analysis of the synthetic case presented in Chapter 3. The value of k_0 is equal to 200 nd.

Table 4 - Parameters Used to Estimate Pressure-dependent Dynamic Permeability

Gangi's model parameters		
Permeability at zero effective stress, k_0	2.00E-04	*md*
m	0.5	
p_1	26000	*psi*
Confining pressure, P_c	15000	*psi*
Effective stress coefficient, α	0.5	

Table 5 - Reservoir Parameters Used in Rate Transient Analysis

Reservoir parameters		
Parameter	**Value**	**Units**
Constant permeability value (*k*)	2.00E-04	*md*
Thickness (*h*)	415	*ft*
Temperature (*T*)	640	*R*
Porosity (φ)	0.06	
Viscosity (μ)	0.0217	*cp*
Total compressibility (c_t)	2.30E-04	*1/psi*
Delta m(p)	8.65E+08	psi^2/cp
Fracture half-length (x_f)	312.5	*ft*
Distance to the boundary (y_e)	100	*ft*
Number of fractures (*n*)	4	

Fig. 6 – 7 show the application of the rate transient analysis for this case. Fig. 6 shows the basic $q_g vs\ t$ log-log plot analysis depicting transient linear flow by its characteristic negative half-slope. Fig. 7 shows the plot used in this analysis, the $\sqrt{t}$ plot. The slope of this plot (m_{cp}) is the most important value to retrieve as it is representative of the production rate data, and is used in the total surface area calculation. The slope of the straight line is 0.00144 $1/D^{1/2}$/Mscf in this case. The final step is to use the reservoir parameters shown in Table 5 and the slope (m_{cp}) of the $\sqrt{t}$ plot to calculate the total fracture surface area. **Table 6** shows 86.5% error between the surface area calculated by the analytical model and the surface area used in the simulation model. The total fracture surface area was significantly under predicted. This large error indicates that using the value of a permeability measured in the absence of stress in a reservoir model yields highly inaccurate results.

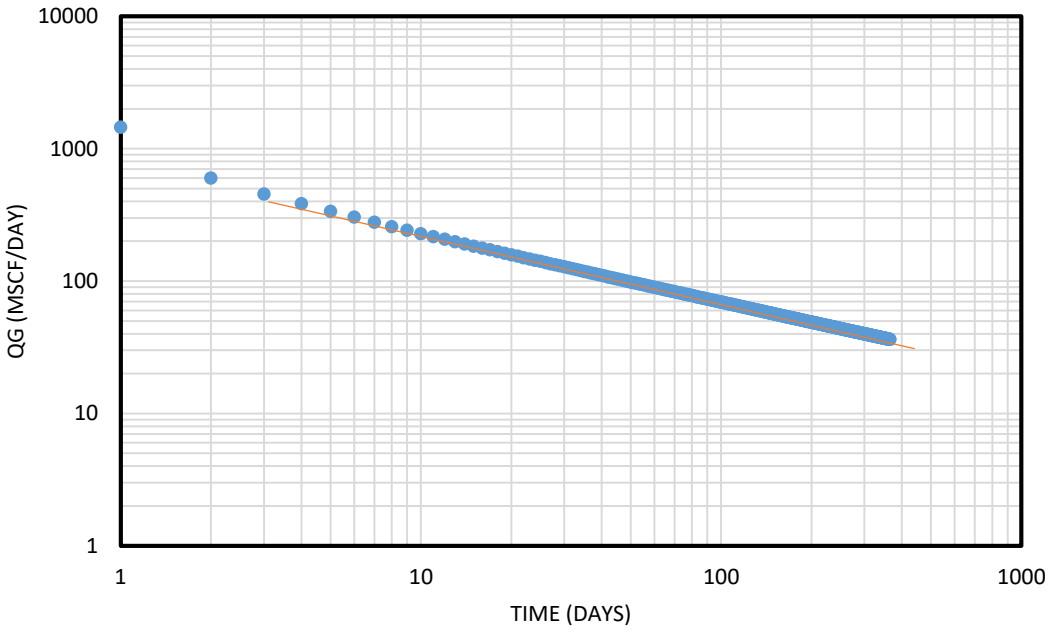

Figure 6 - Log-log plot: Negative Half-Slope Indicates Formation Linear Flow

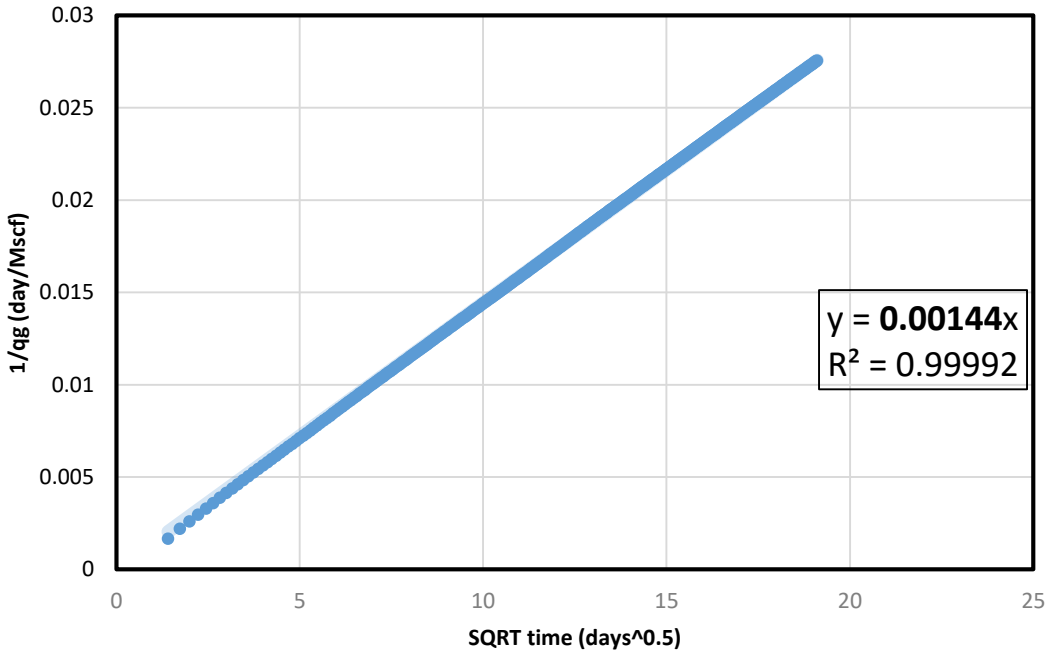

Figure 7 - SQRT Time Plot: m_{cp} = 0.00144 1/D$^{1/2}$/MSCF

Table 6 - Surface Area Calculation Comparison using k_0 as the Reference Permeability Value in the Analytical Model

Surface Area Calculation		
Simulation Model		
$A = 4 \times h \times x_f \times n$	2,075,000 47.64	*ft2* *acres*
Analytical Model		
$A = f_{cp} \times \frac{1261.2 \times T}{\sqrt{(\phi\mu C_t)_i}} \times \frac{1}{m_{cp} \times \sqrt{k} \times \Delta m(p)} \times n$	279,687 6.42	*ft2* *acres*
Error	-86.52	*%*

Since the results above show that using a permeability value measured in the absence of effective stress yields highly inaccurate results with the analytical method, another option must be investigated. The second option is to adjust the permeability measurement for effective stress at initial reservoir conditions; this value will be referred to as k_{init}. In this case, k_{init} is the resulting value of Gangi's permeability (k_m) at initial pore pressure (Wasaki and Akkutlu, 2015). For the specific parameters used in the simulation, $k_{init} = 5\ nd$. Calculation below shows explicitly how k_{init} is estimated.

$$k_{init} = k_m(3800\ psi) = 2e^{-4}\left(1 - \left(\frac{15000 - 0.5 * 3800}{26000}\right)^{0.5}\right)^3 = 5e^{-6}md$$

The simulation results do not change (Fig. 6 and Fig. 7) since the dynamic permeability input is still the same. The only parameter that is changing is the constant permeability value used in the analytical model. The results of using k_{init} as the reference permeability to calculate the total fracture surface area are shown in **Table 7**.

The error between the surface area used in the simulation model and the value calculated by the analytical model is now close to 15%. This means that using a reference value for constant permeability adjusted for effective stress in the reservoir reduced the error in surface area calculation by 71.5%. Since k_{init} proves to be a much better reference value for constant permeability, it will be used in the rest of this thesis as the preferred choice.

Table 7 - Surface Area Calculation Comparison using k_{init} as the Reference Permeability Value in the Analytical Model

Surface Area Calculation		
Simulation Model		
$A = 4 \times h \times x_f \times n$	2,075,000	*ft2*
	47.64	*acres*
Analytical Model		
$A = f_{cp} \times \frac{1261.2 \times T}{\sqrt{(\phi\mu C_t)_i}} \times \frac{1}{m_{cp} \times \sqrt{k} \times \Delta m(p)} \times n$	1,768,898	*ft2*
	40.61	*acres*
Error	-14.75	*%*

4.2.2 Impact of Geomechanical Parameters in the Fracture Surface Area Calculation

Next, a sensitivity analysis was performed to investigate the impact of varying Gangi's parameters on the estimation of total fracture surface area. Each parameter was perturbed independently $\pm 50\%$ from the original value given in Table 4. Each time a new dynamic permeability data was generated and used in the forward simulation. The new production data was used with the analytical model. The error in surface area calculated for each perturbed parameter is given in **Table 8.** Note that the error in surface area ranges from 8.5% to 28%. **Fig. 8** is a more visual representation of the sensitivity analysis as a tornado chart and it shows that p_1 followed by P_c are the most influential parameters affecting the total surface area calculation. p_1 represents the stress required to close the slit-shaped pores and P_c is the confining pressure. When more stress is required to close the pores, the formation permeability is higher. When the confining pressure is lower, the matrix is under less effective stress and thus the formation permeability is higher. This eventually gives a smaller surface area.

As the parameters are perturbed, the value of permeability changes, as well as the degree of stress sensitivity in the formation, which is reflected by the different slopes seen in **Fig. 9**. A steeper slope indicates a stronger reduction of permeability due to the geomechanical characteristics of the formation. Thus, at first glance, one would think that the value of the slope could be related to the degree of error in the surface area calculation. If the slope is steeper, the permeability changes more during the range of pressure of interest and, thus, a higher error is expected in surface area caused by the assumption of constant permeability.

Table 8 - Impact of Gangi's Parameters on Surface Area Calculation Error

Surface Area Calculation									
Simulation Model	2,075,000								ft^2
	47.64								*acres*
Analytical Model	α		m		p_1 (psi)		P_c (psi)		
	0.25	**0.75**	**0.25**	**0.75**	**18,200**	**39,000**	**7,500**	**22,500**	
	1,898,125	1,680,917	1,771,747	1,795,130	1,496,201	1,885,428	1,826,760	1,543,868	ft^2
	43.57	38.59	40.67	41.21	34.35	43.28	41.94	35.44	*acres*
Error	**-8.52**	**-18.99**	**-14.61**	**-13.49**	**-27.89**	**-9.14**	**-11.96**	**-25.60**	%

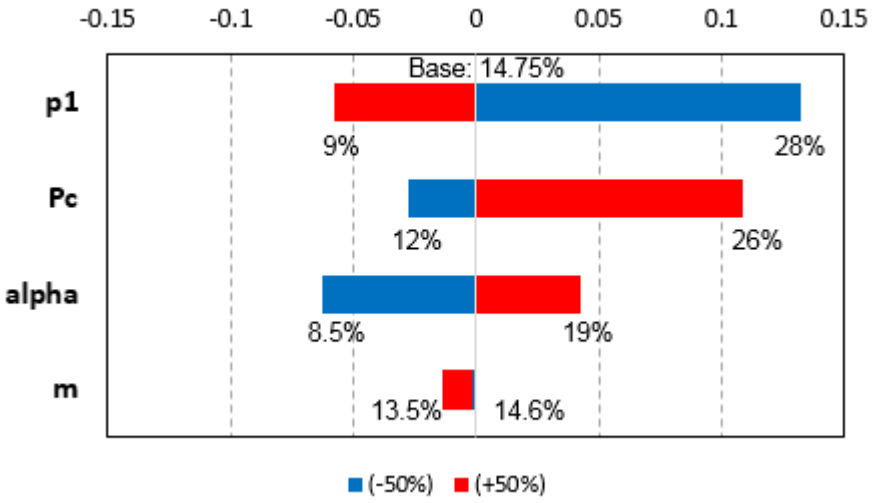

Figure 8 - Impact of Gangi's Parameters on Fracture Surface Area Calculation
*The base error using k_{init} as the constant value in the analytical model is 15%.

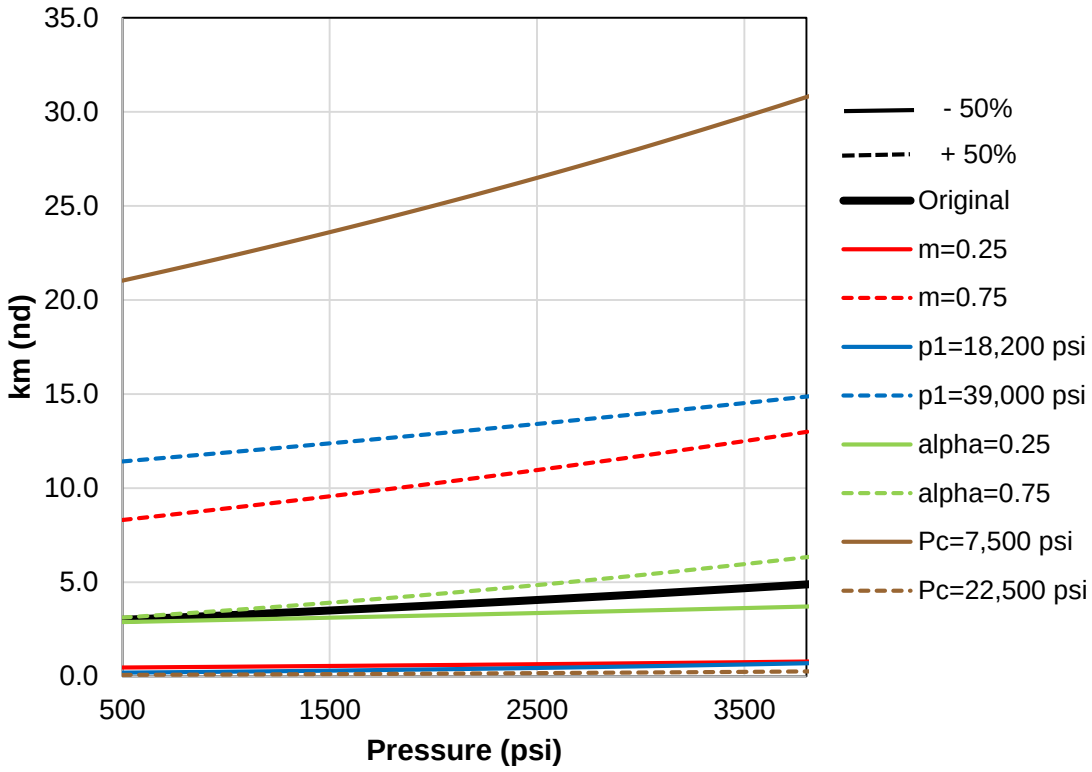

Figure 9 - Sensitivity Analysis: Different Stress Dependence Behavior with Varying Parameters

This hypothesis was analyzed next using **Table 9,** which shows the value of the slope of k_m next to the error in fracture surface area calculated by using a certain parameter value. The steeper slopes are shaded orange and the gentle slopes are shaded green. Similarly, the largest errors on fracture surface area are shaded orange and the smallest errors are shaded green. One would expect to have a correlation between these shaded boxes. For example, the case with the steepest slope is P_c, when perturbed -50%, thus it is shaded orange. One would expect that P_c should yield the highest error in surface area since the permeability is varying the most. However, the error is only 12%. There are other cases yielding errors as high as 28%. The conclusion is

that surprisingly, the results show no correlation between the steepness of the slope, which represents the degree of stress sensitivity of the reservoir, and the magnitude of the error in total fracture surface area. Thus, the error on surface area must be dependent strongly on the value of initial permeability (k_{init}).

A similar analysis was made to determine the impact of k_{init} on the surface area calculation. The higher values of initial permeability where shaded green and the lowest values were shaded orange in **Table 10**. Also, the smaller errors on surface area were shaded green while the higher errors were shaded orange. Results show that there exists a much stronger correlation between the values of k_{init} and error in fracture surface area calculation. The conclusion is that the cases with higher initial permeability have a smaller error in the surface area calculation. This means that the constant permeability assumption is less problematic and induces less error when the matrix permeability is initially high.

The next step in this analysis is to investigate if at the same initial permeability, the steepness of the slope (stress sensitivity) will impact the error on fracture surface area. For example, the case where parameter *m* is perturbed -50% (Case 1) and the case where p_1 is perturbed -50% (Case 2) have roughly the same value of initial permeability, 0.8 and 0.7 nd respectively. Case 1 has a slope in the order of 10^{-5} nd/psi and a surface area error of 14.65%. Case 2 has a slope in the order of 10^{-4} nd/psi and a surface area error of 27.89%. Thus, a steeper slope which indicates higher stress sensitivity of the formation, causes a higher error in the calculation of fracture surface area (as expected in the original hypothesis). Case 1 and Case 2 have a small value of initial permeability, and thus, the same analysis was made with cases with higher permeability values. The results are shown

in **Table 11**. The conclusion is that if the values of initial permeability are constant regardless of the magnitude of the value, then the surface area error will be greater for cases with steeper slopes, which are formations with higher stress-sensitivity.

The main conclusion from the sensitivity analysis of Gangi's parameters on the total fracture surface area calculation is that the error caused by the constant permeability assumption is primarily dependent on the initial permeability value. There will be more error introduced in the model for shale matrix with low initial permeability. The degree of stress sensitivity within the reservoir is of less importance. However, in the case that the initial permeability is constant, the higher stress sensitivity will cause a higher error on the total surface area calculation.

Table 9 - Analysis of the Impact of Stress-Sensitivity of the Formation on the Fracture Surface Area Calculation

Parameter	(+50%)		(-50%)	
	slope (nd/psi)	Error in SA (%)	slope (nd/psi)	Error in SA (%)
m	1.42E-03	13.49%	9.09E-05	14.65%
α	9.70E-04	18.99%	1.82E-04	8.52%
p_1	1.06E-03	9.14%	1.52E-04	27.89%
P_c	6.06E-05	25.60%	2.97E-03	11.96%

Table 10 - Analysis of the Impact of Initial Permeability on the Fracture Surface Area Calculation

Parameter	(+50%)		(-50%)	
	k_{init} (nd)	Error in SA (%)	k_{init} (nd)	Error in SA (%)
m	13	13.49%	0.8	14.65%
α	6.3	18.99%	3.7	8.52%
p_1	14.9	9.14%	0.7	27.89%
P_c	0.3	25.60%	30.8	11.96%

Table 11 - Analysis of the Impact of Stress-Sensitivity When the Initial Permeability is Constant

		k_{init} (nd)	slope (nd/psi)	Error in SA (%)
Case 1	m (-50%)	0.8	9.09E-05	14.65%
Case 2	p_1 (-50%)	0.7	1.52E-04	27.89%
Case 1	α (+50%)	6.3	9.70E-04	18.99%
Case 2	α (-50%)	3.7	1.82E-04	8.52%
Case 1	m (+50%)	13	1.42E-03	13.49%
Case 2	p_1 (+50%)	14.9	1.06E-03	9.14%

4.3 Wasaki's Organic-Rich Shale Permeability Model

As explained in the introduction, the shale matrix is comprised of two different types of pores: inorganic slit-shaped pores and organic round pores. Gangi's model is able to describe the stress-dependent permeability in the inorganic matrix, but it does not consider the presence of organic pores. Wasaki and Akkutlu (2015) developed an apparent permeability model (**Eq. 4.2**) that describes the permeability taking into account molecular transport mechanisms in the organic pores.

$$k_{gas} = k_m + \mu D c_g + \mu D_s \frac{V_{SL}\rho_{grain}B_g}{\varepsilon_{ks}} \frac{p_L}{(p+p_L)^2} \tag{4.2a}$$

$$k_m = k_0 \left[1 - \left(\frac{P_c - \alpha p}{P_1}\right)^m\right]^3 \tag{4.2b}$$

The first term describes stress-sensitive convection (inorganic pores), the second term represents the free gas molecular diffusion (organic and inorganic pores) and the third term accounts for the sorbed-phase diffusion (organic pores). Both molecular and sorbed-phase diffusion are modeled using Fickian diffusion, which means that they are non-Darcian mechanisms. For further details on the derivation of the apparent permeability model, refer to Wasaki (2015).

Wasaki and Akkutlu (2015) performed a sensitivity analysis on cumulative gas production and concluded that the most important parameters in the apparent gas permeability model are those associated with geomechanics (Gangi's parameters): *m* and p_1.

In this section, the apparent permeability model given in Eq. 4.2 was used as the dynamic permeability model in the simulation. The parameters used in the simulation model are shown in **Table 12**. The pressure-dependent input to the simulation are shown in **Table 13**.

The analysis of formation linear flow using $k_{init} = 5nd$ was conducted for the production results obtained from the simulation model using Wattenbarger's square root of time plot method (1998). **Fig. 10** shows the log-log plot where formation linear flow is identified by a negative half-slope. **Fig. 11** is $\sqrt{t}$ plot, which is the most critical plot as it yields the value of the constant pressure slope, m_{cp}= 0.00093 1/D$^{1/2}$/MSCF**.** This slope value is used to calculate the total fracture surface area as shown in **Table 14**. The constant permeability assumption results in a 32% error in total fracture surface area for this dynamic permeability model. The error increased from 15% when using Gangi's model to 32% when using Wasaki's apparent permeability model. This indicates a 17% additional error due to molecular transport effects. This argument will be re-visited in this section.

This study will investigate the impact of the geomechanical, molecular transport and sorbed phase parameters in the calculation of total fracture surface area to identify which parameters affect the area calculation the most. Following Wasaki and Akkutlu (2015) sensitivity analysis procedure, the impact of the nine parameters in the apparent permeability model was studied. Each parameter was perturbed $\pm 50\%$ independently to investigate the effect on the total fracture surface area calculation. **Table 15** shows the parameters used for the analysis, their base value and their perturbed range.

Table 12 - Parameters Used to Calculate Organic-Rich Permeability

Reservoir properties		
Temperature, *T*	640	*R*
Initial pore pressure, *p*	3800	*psi*
Pore compressibility, *Cpp*	3.00E-06	*1/psi*
Porosity, φ	0.06	
Sorption properties		
Grain density, ρ_{grain}	166	*lbm/cft*
Bulk density, ρ_b	156	*lbm/cft*
Organic volume per total grain volume, ε_{ks}	0.01	
Langmuir volume, V_{sL}	100	*scf/ton*
Langmuir pressure, p_L	2000	*psia*
Gangi's model parameters		
Permeability at zero effective stress, k_0	2.00E-04	*md*
m	0.5	
p_1	26000	*psi*
Confining pressure, P_c	15000	*psi*
Effective stress coefficient, α	0.5	
Gas properties		
Composition	Methane 100%	
Molecular weight, M	16	*lbm/lb-mol*
Specific gravity	0.6	
Free gas density at standard condition, $\rho_{sc,gas}$	0.04	*lbm/cft*
Molecular diffusion coefficient, *D*	1.00E-09	*m2/s*
Surface diffusion coefficient, *Ds*	1.00E-09	*m2/s*

Table 13 - Pressure-dependent Properties Used for Forward Simulation

Pressure	*Z-factor*	*Viscosity (cp)*	*k gas (md)*
500	0.963733915	0.013669201	2.57847E-05
700	0.950860317	0.013941863	1.76362E-05
900	0.939122689	0.014253261	1.34611E-05
1100	0.928655711	0.01460129	1.10269E-05
1300	0.919585331	0.01498432	9.49159E-06
1500	0.912021194	0.015400666	8.47185E-06
1700	0.906049181	0.015848335	7.77042E-06
1900	0.90172527	0.016324923	7.27673E-06
2100	0.89907184	0.016827618	6.92475E-06
2300	0.898077125	0.017353283	6.6731E-06
2500	0.898697843	0.017898574	6.4948E-06
2700	0.900864355	0.018460085	6.37174E-06
2900	0.904487312	0.01903448	6.29137E-06
3100	0.909464623	0.019618594	6.24482E-06
3500	0.92304755	0.020804631	6.22914E-06
3800	0.935986056	0.021700204	6.26923E-06

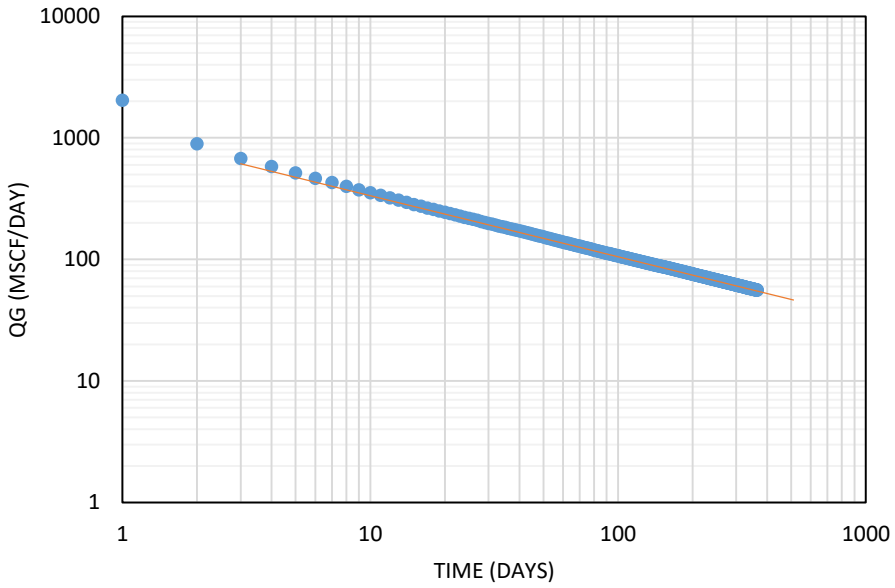

Figure 10 - Log-log plot: The Shale Gas Well is in Transient Linear Flow After 1 Year of Production

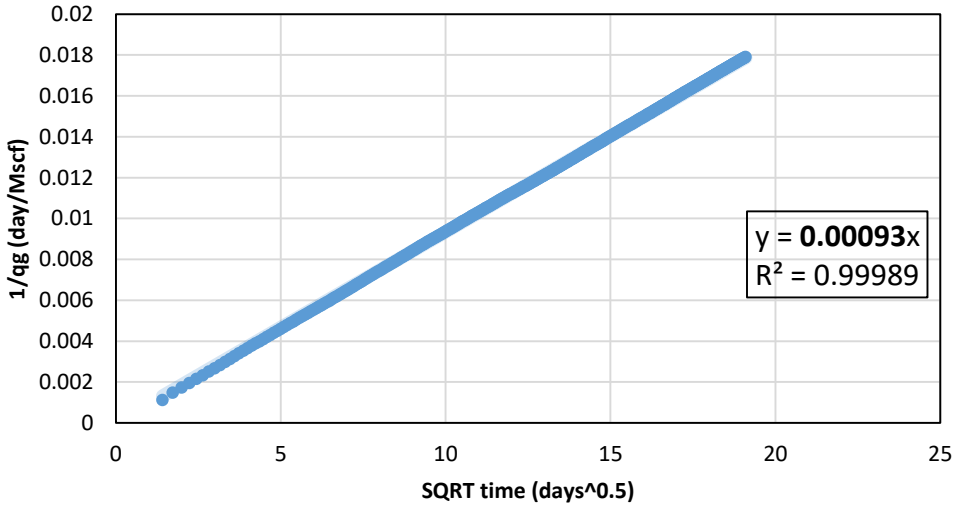

Figure 11 - SQRT Time Plot: m_{cp} = 0.00093 1/D$^{1/2}$/MSCF

Table 14 - Surface Area Calculation Comparison Using Organic-Rich Permeability Model

Surface Area Calculation		
Simulation Model		
$A = 4 \times h \times x_f \times n$	2,075,000	*ft2*
	47.64	*acres*
Analytical Model		
$A = f_{cp} \times \frac{1261.2 \times T}{\sqrt{(\phi \mu C_t)_i}} \times \frac{1}{m_{cp} \times \sqrt{k} \times \Delta m(p)} \times n$	2,738,939	*ft2*
	62.88	*acres*
Error	+32.00	*%*

Table 15 - Parameters Used in Sensitivity Analysis

Parameters		Unit	Base	Range
Geomechanics	α	-	0.5	0.25 ~ 0.75
	m	-	0.5	0.25 ~ 0.75
	p_1	psi	26,000	18,300 ~ 39,000
	P_c	psi	15,000	7,500 ~ 22,500
Molecular Transport	D	m^2/s	1.00E-09	0.5E-9 ~1.5E-9
	D_s	m^2/s	1.00E-09	0.5E-9 ~1.5E-9
Sorption Parameters	ε_{ks}	-	0.01	0.005 ~ 0.015
	p_L	psi	2,000	1,000 ~ 3,000
	V_{sL}	scf/ton	100	50 ~ 150

4.3.1 Impact of Geomechanical Parameters in Fracture Surface Area Calculation

The first category of parameters to investigate are those describing the stress-sensitive permeability of the formation, referred to as k_m in Eq. 4.2. **Table 16** shows the numerical results of the variation in fracture surface area calculation according to each parameter perturbed. The error caused by assuming a constant permeability in this analysis ranges from 7% to 323%.

Fig. 12 is a tornado plot representing the error variation visually. The y-axis corresponds to the perturbed parameters and the x-axis shows the impact on the error of total fracture surface area as a fraction. Zero in the center represents no difference from the base case (which corresponds to an error of 32%). For example, the first parameter is P_c ; the blue bar corresponds to the case where P_c was perturbed -50%. The length of the bar indicates that the error in the surface area calculation decreased by 29%. Similarly, the red bar corresponds to the case where P_c was perturbed +50%. The magnitude of the red bar indicates that the error on the surface area calculation increased by 290%.

The results show that the fracture surface area calculation is most sensitive to P_c. P_c is the confining pressure; thus, when the value of P_c is reduced, the effective stress exerted on the matrix is reduced as well, which causes the permeability to increase significantly. Consequently, the surface area predicted is smaller. Conversely, when the confining pressure increases, so does the effective stress exerted on the formation, and hence the permeability decreases. The effect of P_c on permeability can be seen in **Fig. 13**. p_1 and m are also producing a wide range of error, but not as high as compared to P_c . p_1 is the effective stress required to close slit-shaped pores completely. Thus, the higher p_1

value, the higher resistance the matrix has against the applied effective stress, and this results in a higher formation permeability as shown in **Fig. 14**. *m* is a parameter associated with the surface roughness of the pores. If the value of *m* is close to unity, the surface is smooth since the height of the asperities is uniform. This results in a higher permeability as shown in **Fig. 15**, since the uniformity in height makes the slit-shaped pore more resistant to effective stress. In the contrary, if the value of *m* is close to zero, the pore has a larger range of asperity height and thus it is easier for the pores to close during gas production (higher effective stress). Also, it is important to notice that the value of the stress coefficient (α) has a minor influence since there is no large variation in the permeability curves as the value of α is being perturbed as shown in **Fig. 16**.

Table 16 - Impact of Geomechanical Parameters in Fracture Surface Area Calculation

Surface Area Calculation									
Simulation Model									
	2,075,000								ft^2
$A =$	47.64								*acres*
Analytical Model	**alpha**		**m**		**p1 (psi)**		**Pc (psi)**		
	0.25	**0.75**	**0.25**	**0.75**	**18,200**	**39,000**	**7,500**	**22,500**	
	3,052,655	2,521,375	5,419,460	2,224,950	5,626,210	2,228,234	2,005,854	8,769,168	ft^2
$A =$	70.08	57.88	124.41	51.08	129.16	51.15	46.05	201.31	*acres*
Error	**+47.12**	**+21.51**	**+161.18**	**+7.23**	**+171.14**	**+7.38**	**-3.33**	**+322.61**	*%*

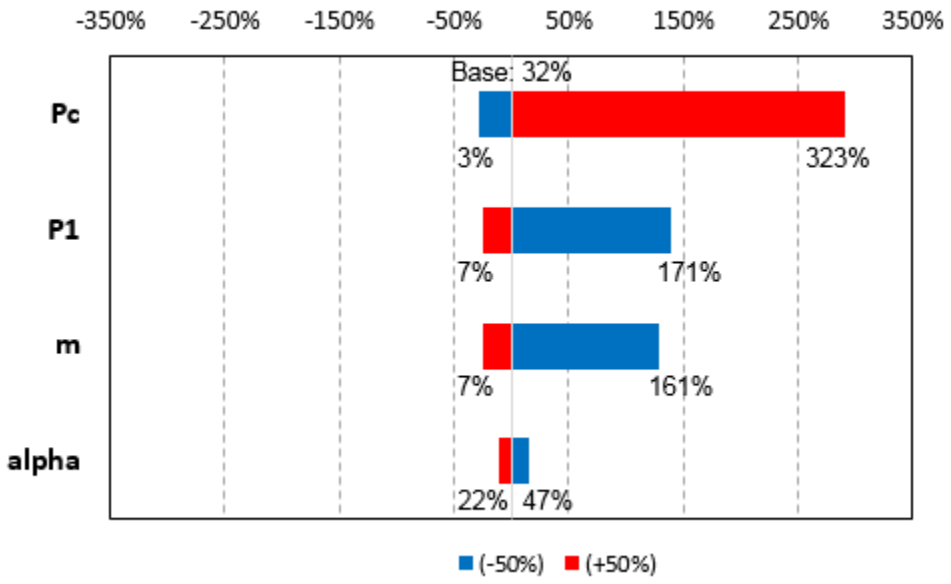

Figure 12 - Sensitivity of Geomechanical Parameters on Total Fracture Surface Area Calculation

*The base error using k_{init} as the constant value in the analytical model is 32%.

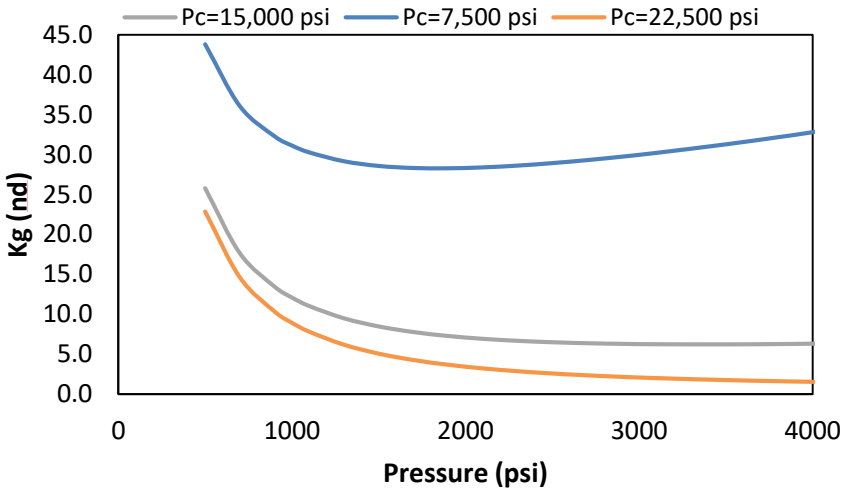

Figure 13 - Impact of Confining Pressure in k_{gas}

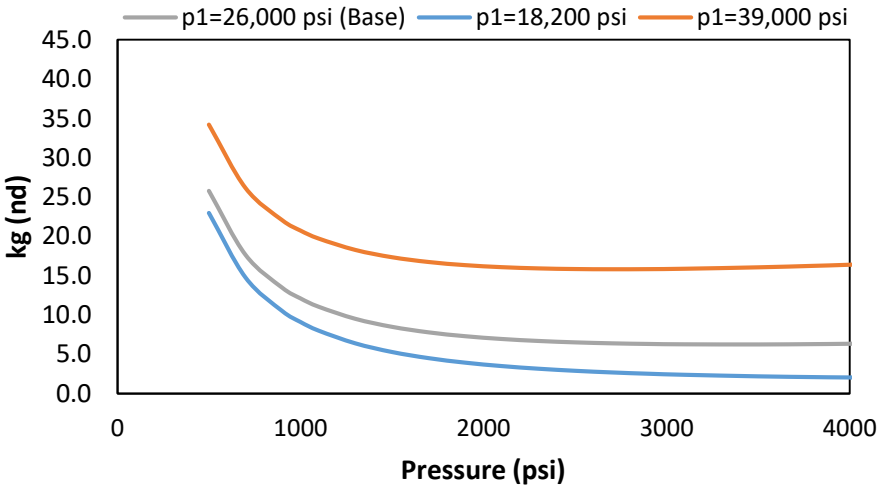

Figure 14 - Impact of Parameter p_1 in k_{gas}

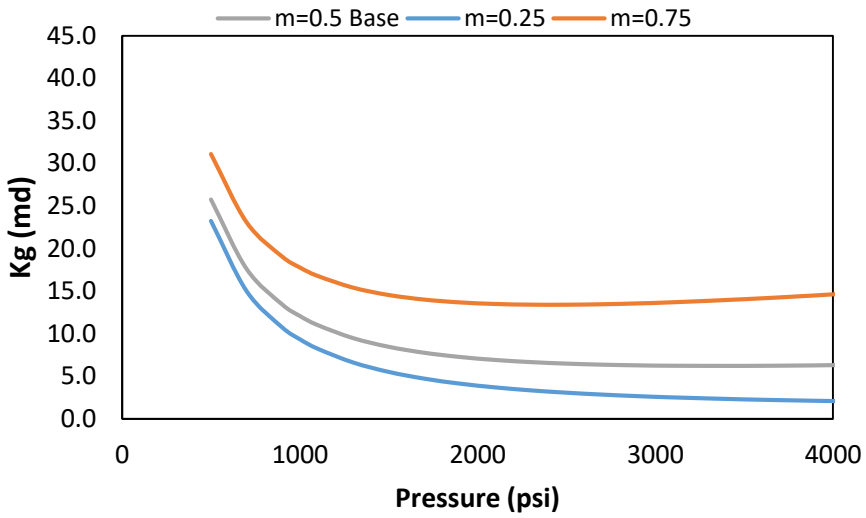

Figure 15 - Impact of Parameter m in k_{gas}

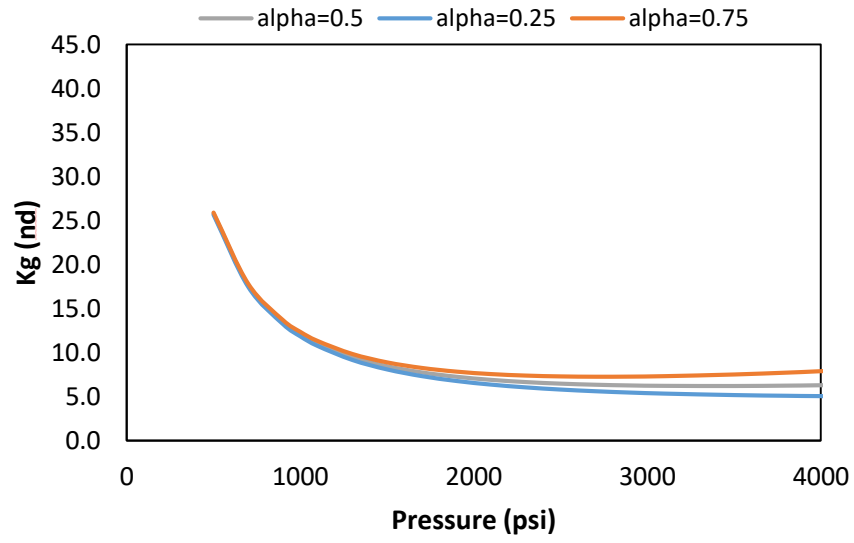

Figure 16 - Impact of Effective Stress Coefficient (α) in k_{gas}

4.3.2 Impact of Molecular Transport Parameters in Fracture Surface Area Calculation

The second category of parameters in the apparent permeability model are those which describe molecular transport. $\boldsymbol{D}$ is the pore diffusion coefficient, which applies for the "free" gas in the inorganic pores and the center of the organic pores. $\boldsymbol{D_s}$ refers to the sorbed diffusion coefficient, which applies for the gas stored in adsorbed state close to the organic pore walls. The sensitivity analysis of these parameters was conducted following the same procedure applied to the geomechanical parameters. Each parameter was perturbed independently $\pm$50 % and the results for total fracture surface area calculation are shown in **Table 17**. The error caused by assuming a constant permeability ranges from 18% to 42%. Even though this is a wide range of error, when comparing it with the range of error resulting from perturbing the geomechanical parameters, it is obvious that this category influences the surface area calculation much less.

Table 17 - Impact of Molecular Transport Parameters in Surface Area Calculation

Surface Area Calculation						
Simulation Model						
$A = 4 \times h \times x_f \times n$	2,075,000					ft^2
	47.64					*acres*
Analytical Model	**D (m2/s)**		**Ds (m2/s)**			
$A = f_{cp} \times \frac{1261.2 \times T}{\sqrt{(\phi\mu C_t)_i}} \times \frac{1}{m_{cp} \times \sqrt{k} \times \Delta m(p)} \times n$	**5.00E-10**	**1.50E-09**	**5.00E-10**	**1.50E-09**		ft^2
	2,599,197	2,830,237	2,449,243	2,961,876		*acres*
	59.67	64.97	56.23	68.00		
Error	**+25.26**	**+36.40**	**+18.04**	**+42.74**		%

Fig. 17 shows the relative impact on the surface area error, where it is shown that the sorbed diffusion coefficient ($\boldsymbol{D_s}$) has a stronger impact on the surface area calculation than the pore diffusion coefficient ($\boldsymbol{D}$). This can be explained by looking at how the apparent permeability model changes when these parameters are varied. **Fig. 18** shows that when $\boldsymbol{D_s}$ is perturbed, there is a significant variation in matrix permeability at lower pressures. This permeability variation causes the error on surface area to decrease by 14% with a smaller value of D_s, and to increase by 11% with a higher value of D_s. In contrast, the effect on permeability of perturbing D is not very significant. The apparent permeability curves look very similar in the entire range of pressures as shown in **Fig. 19.** Thus, the error on surface area decreases only by 6% when using a smaller value of D and increases by 4% when using a higher value of D. It is important to remember that the base case resulted in an error of 32% due to the assumption of constant permeability.

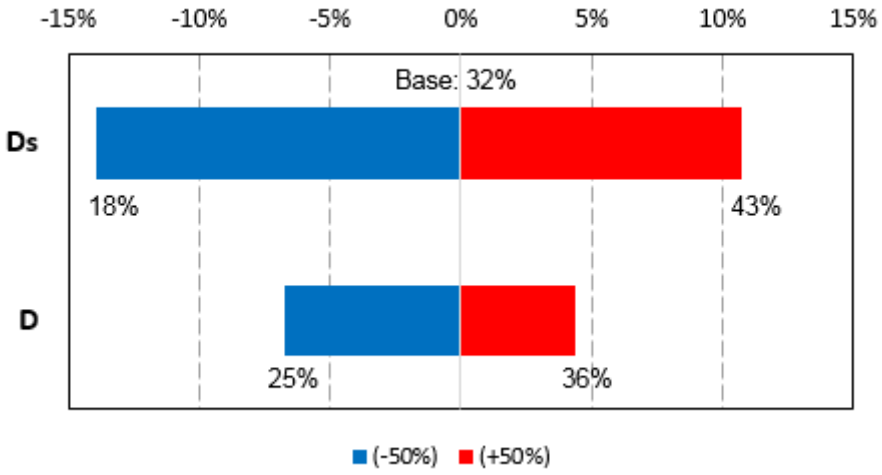

Figure 17 - Sensitivity of Molecular Transport Parameters on Total Fracture Surface Area Calculation

*The base error using k_{init} as the constant value in the analytical model is 32%.

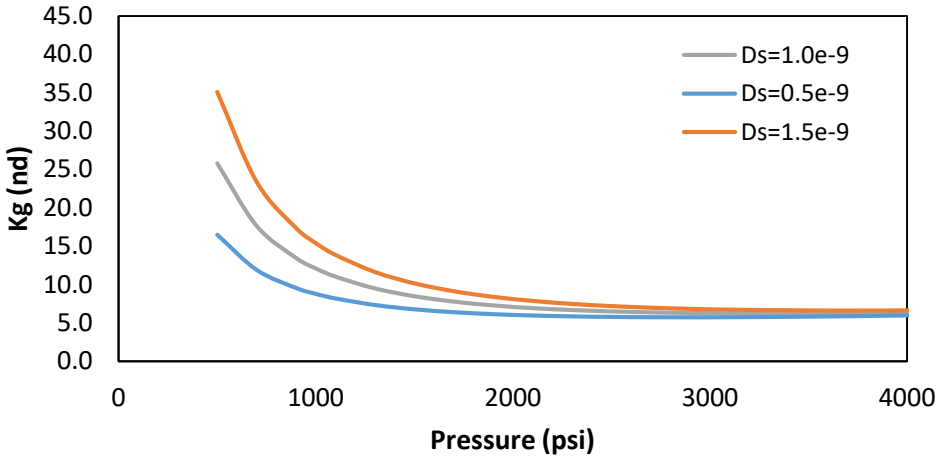

Figure 18 - Impact of Surface Diffusion Coefficient in k_{gas}

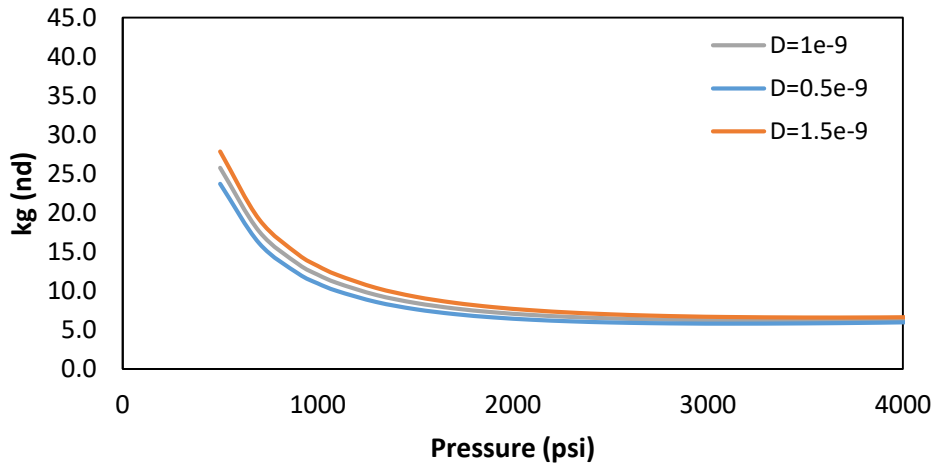

Figure 19 - Impact of the Molecular Diffusion Coefficient in k_{gas}

4.3.3 Impact of Sorption Parameters in Fracture Surface Area Calculation

The last category of parameters included in the apparent permeability model is the sorption parameters. As explained before, these parameters describe the nature of the flow of the sorbed-phase in organic pores. It is expected that the sorption parameters enhance the permeability at low pressures. The question is if this enhancement in permeability in the low pressure range is enough to significantly affect the surface area calculation. In order to investigate this question, a similar sensitivity analysis has been performed by perturbing the sorption parameters independently $\pm$50%. **Table 18** and **Fig. 20** show that varying the sorption parameters result in a range of error between 1% and 64%. Table 18 shows that when the organic content is higher, the error in the calculated fracture surface area is reduced to 23%. In contrast, when the value for organic content is low, the error in surface area increases up to 55%. This can be explained by looking at the effect of organic content on apparent permeability. **Fig. 21** shows that a lower value of organic content results in a large increase in apparent permeability at low pressures. Thus, since the difference between the apparent permeability and the constant value assumed in the analytical model is higher, the error in surface area calculation increases. The most influential parameter is Langmuir volume (V_{sL}). Wasaki (2015) explains that V_{sL} is the only parameter out of the nine parameters that were perturbed that has an impact on storage as well as deliverability. **Fig. 22** shows that a larger value of V_{sL} increases apparent permeability at lower pressures significantly; thus, it has a positive impact on deliverability. This result agrees with Wasaki's observations. However, Wasaki (2015) also showed that as this parameter increases, the percentage of gas volume that can be

recovered decreases, which is an important consideration for production forecast. Finally, p_L was the parameter with less impact in the surface area calculation. The error increased by 1% with the smaller value of p_L and it decreased by 4% with the larger value of p_L. It is important to mention that this effect on error was produced by the permeability enhancement seen at lower pressures (**Fig. 23**).

The results discussed in this section agree with the original premise that sorption parameters enhance formation permeability at low pressures but have a negligible effect at high pressures. However, the study of sensitivity on the total surface area calculation error demonstrates that this enhancement in permeability is translated to higher errors when the sorption effects are ignored.

Table 18 - Impact of Sorption Parameters in Surface Area

Surface Area Calculation							
Simulation Model							
$A =$	2,075,000						*ft2*
	47.64						*acres*
Analytical Model	**εks**		**pL (psi)**		**VsL (scf/ton)**		
	0.005	**0.015**	**1,000**	**3,000**	**50**	**150**	
$A =$	3,224,320	2,547,213	2,768,710	2,653,347	2,054,204	3,396,284	*ft2*
	74.02	58.48	63.56	60.91	47.16	77.97	*acres*
Error	**+55.39**	**+22.76**	**+33.43**	**+27.87**	**-1.00**	**+63.68**	*%*

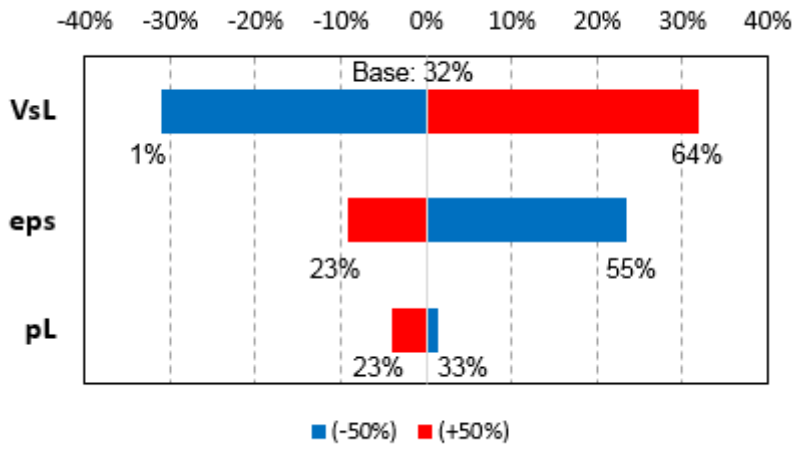

Figure 20 - Sensitivity of Sorption Parameters on Total Fracture Surface Area Calculation

*The base error using k_{init} as the constant value in the analytical model is 32%.

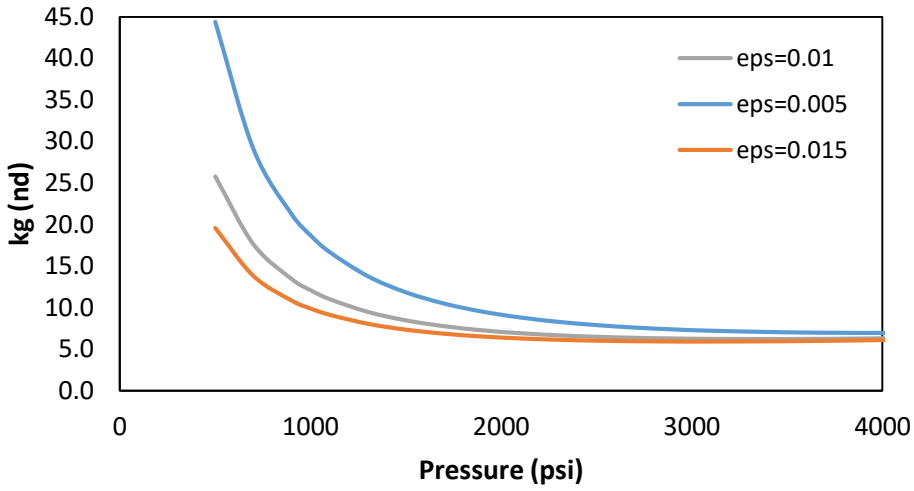

Figure 21 - Impact of Organic Volume Percentage (ε_{ks}) in k_{gas}

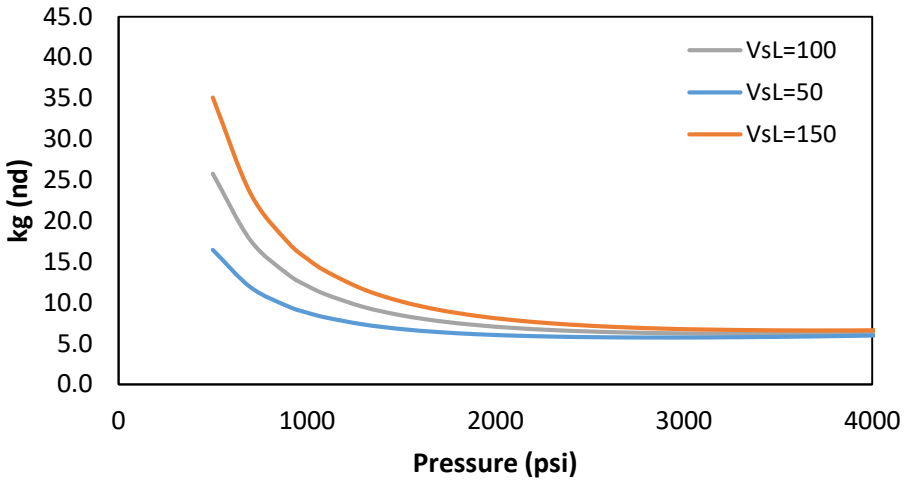

Figure 22 - Impact of Langmuir Volume in k_{gas}

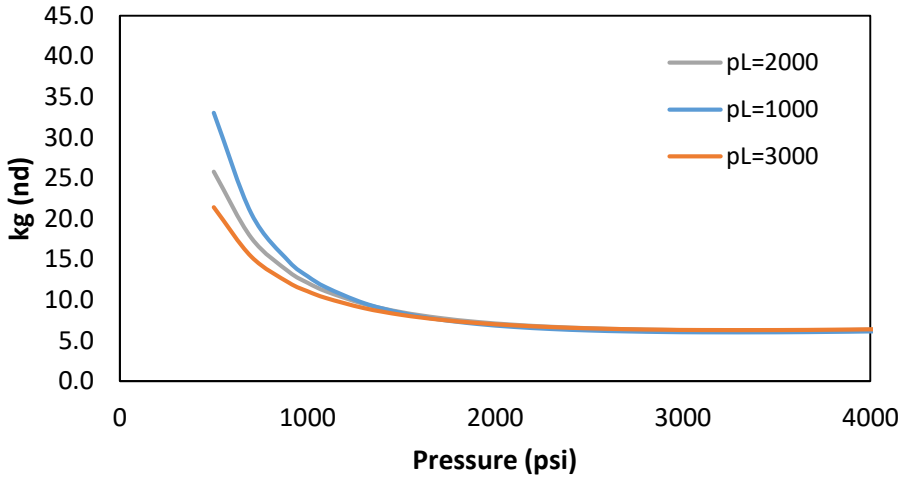

Figure 23 - Impact of Langmuir Pressure in k_{gas}

4.3.4 Impact of Dynamic Permeability Near and Away from the Fracture

The previous section focused on analyzing how the parameters in the apparent permeability model impact the total fracture surface area calculation. The main reason behind this variable effect is that each parameter changes the apparent permeability curve differently as they are perturbed. Some parameters have more impact at high pressures, while others only make a difference at low pressures. The focus of this section is analyzing the effect of perturbing the same parameters on the apparent permeability curve and how this variation is tied to the error in total fracture surface area previously discussed.

In order to perform this analysis, the deviation of k_{gas} between the model with the original inputs (Table 9) and the model with each perturbed parameter has been calculated using **Eq. 4.3**. Thus, the results are shown in fraction form.

$$k_g\ deviation = \frac{k_{gas} - k_{gas}(base)}{k_{gas}(base)} \tag{4.3}$$

The nine parameters used in the sensitivity analysis can be divided in two main categories based on the pressure range where the impact is significant which in turn defines the position with respect to the fracture where the effects come into play. The stress-sensitivity parameters, also referred to as the geomechanical parameters, influence the apparent permeability model in a greater degree at high pressures, which corresponds to the area away from the fractures as shown in **Fig. 24**. From the discussion in the last section, it was determined that the geomechanical parameters are the ones which influence the total fracture surface area calculation the most. Thus, it can be established that this large impact represented by a wide range of errors in surface area, comes from the

deviation of k_{gas} in the area away from the fractures. Another observation is that the error decreases as the permeability increases (positive k_{gas} deviation). For three of the parameters: 1) the effective stress coefficient, α, 2) m, which is associated with pore surface roughness and 3) p_1, which is the effective stress at which the pores close completely, a permeability increase and a smaller error on surface area occur when the value of the parameter is increased. Conversely, confining pressure (P_c) has the opposite effect on k_{gas}. As the value for P_c decreases, apparent permeability increases, yielding a smaller error on surface area calculation. These results agree with the conclusion of the analysis on the sensitivity of parameters on Gangi's model, which show that as the value of initial permeability increases, a smaller error on fracture surface area is obtained from the analytical model.

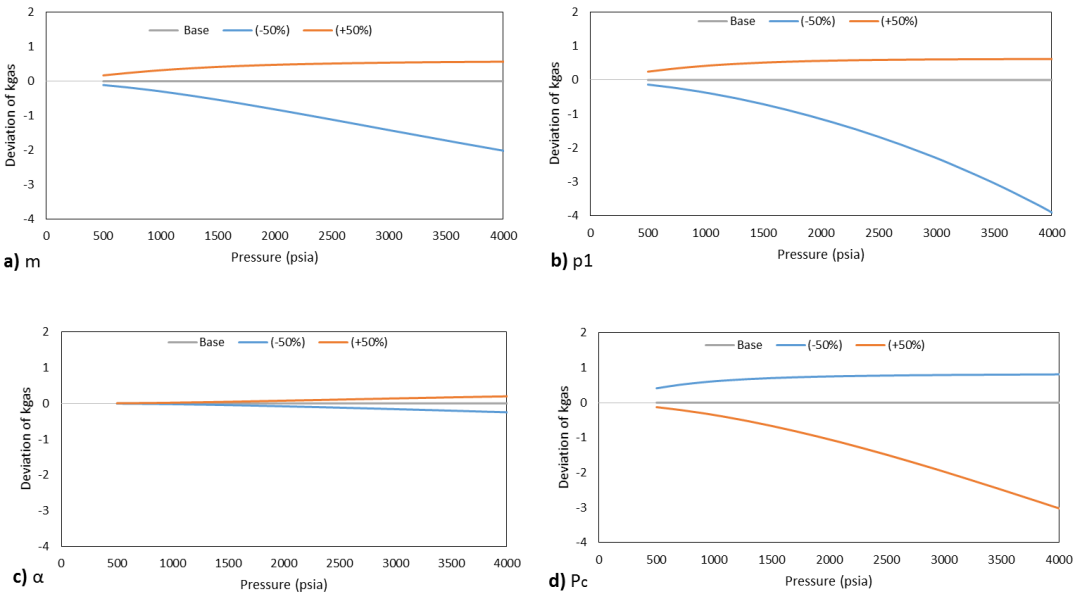

Figure 24 - Sensitivity of Mechanical Parameters in k_{gas}

The second category includes the molecular transport parameters as well as the sorption parameters. These have the opposite effect on the apparent permeability model as they change the value of k_{gas} primarily at low pressures, which corresponds to the area near the fractures as shown in **Fig. 25**. In this case, a higher apparent permeabilty causes the error on surface area to be greater when compared to the base case scenario. The pore diffusion coefficient (D), sorbed diffusion coefficient (D_s) and Langmuir Volume (V_{sL}) follow the same trend. An increase in the value of these parameters results in a higher k_{gas} and thus, in a higher error in total fracture surface area. In contrast, a smaller value of organic content (ε_{ks}) and Langmuir pressure (p_L) increases k_{gas} and in turn, the error in total fracture surface area. As mentioned before, these errors in surface area come from an enhancement in permeability near the fractures.

It is important to discuss Fig. 25 further. Based on Gangi's analysis shown on Section 4.2, the variation in error from one case to another depends on the value of initial permeability. In the case of molecular and sorption parameters, initial permeability remains unchanged as each parameter is perturbed. Thus, this would imply that the error should remain the same for each parameter. However, this is not the case, and the error ranges from 1% to 64% for sorption parameters and 18% to 43% for molecular transport parameters. This variation in error is coming from the effects of molecular transport near the fracture. As seen in Fig. 25, the permeability curve is only changing slightly near the fracture (low pressures), but even these slight variations are causing the error to vary significanlty. Thus, the molecular effects have an important impact in the calculation of total surface area and should not be ignored.

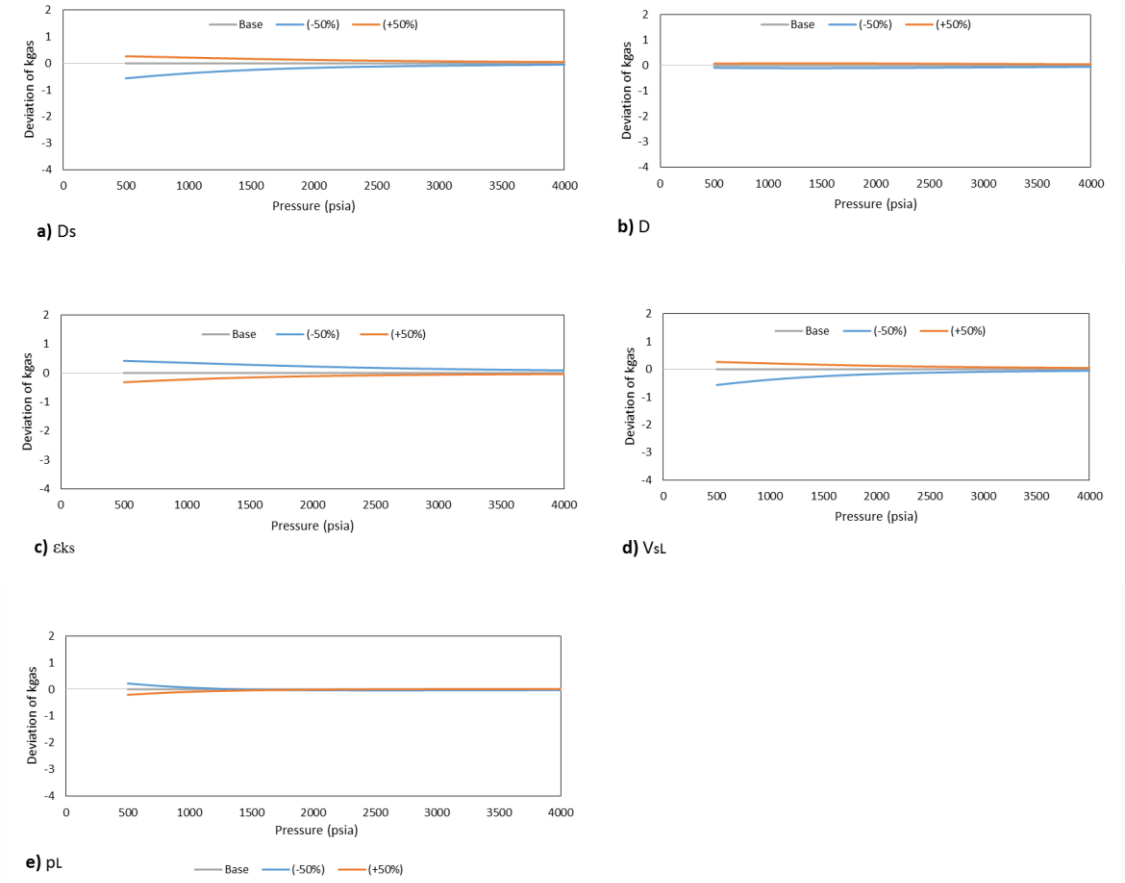

Figure 25 - Sensitivity of Molecular Transport and Sorption Parameters in k_{gas}

4.3.5 Conclusion on Sensitivity Analysis

The results of the sensitivity analysis show that the parameters that have the highest impact on the total fracture surface area calculation are those associated with geomechanics. As seen in **Fig. 26**, the three highest ranked parameters are P_c, p_1 and m, respectively, as part of Gangi's model, which is used in this study to describe the stress-dependency of the slit-shaped pores in the inorganic matrix. Also, the analysis confirmed that these wide range of errors come from ignoring the dynamic permeability away from the fractures. The second most influential category is the sorption parameters: V_{sL} and ε_{ks}, which are ranked fourth and fifth, respectively. The impact of these parameters on the surface area calculation comes from ignoring the dynamic permeability of the matrix near the fractures.

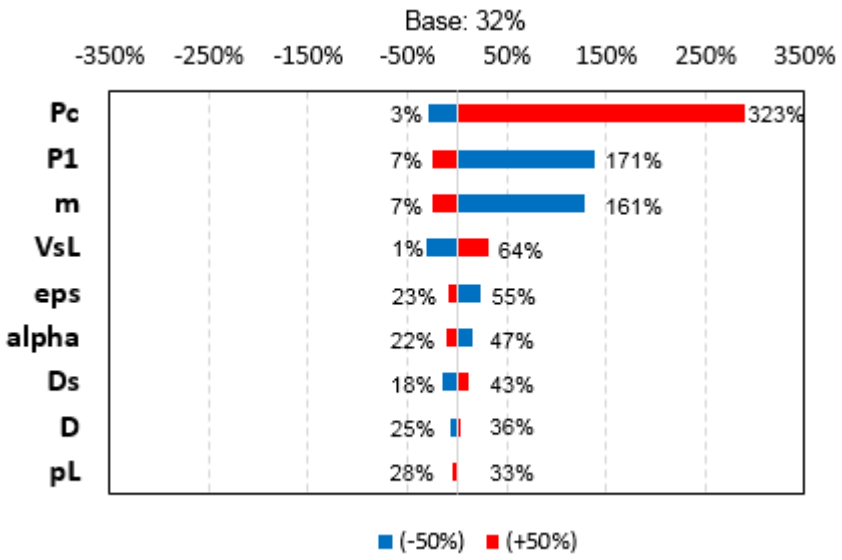

Figure 26 - Impact of Parameters on Total Fracture Surface Area Calculation
*****The base error using k_{init} as the constant value in the analytical model is 32%.

CHAPTER V

TOTAL FRACTURE SURFACE AREA MODEL REVISITED FOR DYNAMIC PERMEABILITY

5.1 Pseudo-pressure and Pseudo-time Discussion

As demonstrated in the previous chapter, there is a significant error caused by assuming that formation permeability is a constant parameter. Thus, this thesis re-visits transient linear flow theory (Wattenbarger et al., 1998) to modify the model to incorporate dynamic formation permeability.

It is well known that fluid compressibility (z) and viscosity (μ) are dependent on pressure when dealing with gas flow. These pressure-dependent gas properties introduce non-linearity to the diffusivity equation, and thus, different solutions have been proposed in order to linearize the equation. The more general solution involves the definition of pseudo-pressure which accounts for the pressure-dependent gas properties. Similar to gas compressibility and viscosity, in this study we include formation permeability as a pressure-dependent property. Thus, it should be included in the definition of real gas pseudo-pressure as shown in **Eq. 5.1.**

$$m_k(p) = 2\int_{P_b}^{P} \frac{k_{gas}\, p}{z\mu}\, dp \tag{5.1}$$

Including permeability in the definition of pseudo-pressure linearizes the left-hand side of the diffusivity equation as shown in **Eq. 5.2** using field units; however, the

right-hand side of the equation is still dependent on permeability, viscosity and total compressibility.

$$k_m = k_0 \left[1 - \left(\frac{P_c - \alpha p}{P_1}\right)^m\right]^3 \tag{5.2}$$

Thus, the introduction of pseudo-time is necessary to linearize the equation entirely. The concept of pseudo-time was originally developed by Agarwal (1979). Since then, alternative definitions of pseudo-time have been developed; however, the constant permeability assumption has been maintained in the derivations. To account for dynamic permeability, it is necessary to include permeability in the definition of pseudo-time as shown in **Eq. 5.3**. However, a proper discussion on the selection of which definition of pseudo-time to use is needed.

$$t_{ap} = \sum_{j=1}^{n} \frac{k_{gas}}{(\mu C_t)_j} \Delta t_j \tag{5.3}$$

Agarwal (1979) introduced the concept of pseudo-time for the first time for transient flow. The definition presented is shown in **Eq. 5.4**. The purpose of pseudo-time is to improve the accuracy of analytical solutions by considering the effects of pressure-dependent gas viscosity and compressibility, which are, in turn, a function of time. Introducing pseudo-time requires an integration (**Eq. 5.5**) that can be performed using midpoint rule: reading the midpoint values of $\frac{1}{\mu C_t}$ from the table and multiplying by the pressure difference.

$$t_a(p) \approx \sum_{j=1}^{n} \frac{\Delta t_j}{(\mu C_t)_j} \tag{5.4}$$

$$\frac{1}{(\mu C_t)_j} = \frac{1}{\Delta p_j} \int_{p_{j-1}}^{p_j} \frac{dp}{\mu(p)\, C_t(p)} \tag{5.5}$$

The benefit of using the pseudo-time transformation is that since viscosity and compressibility are already accounted for in the derivation of pseudo-time, then these parameters are not present in the dimensionless definitions of rate and time as shown later in this discussion.

Fraim and Wattenbarger (1987) modified the original definition of pseudo-time to develop a normalized time that linearizes the gas rate decline vs. normalized time for a gas well producing at fixed bottom-hole pressure in boundary-dominated flow (**Eq. 5.6**). In this case, the product μC_t must be evaluated at average pressure. Their method makes gas propertied behave as liquid and uses exponential decline after the boundary has been reached.

$$t_n = \int_0^t \frac{(\mu C_t)_i}{\mu(\bar{p}) C_t(\bar{p})}\, dt \tag{5.6}$$

The weakness of this method is that in order to obtain normalized time, an iterative process must be followed. Thus, it is necessary to assume a value for original gas in place, G, to get average pressure $(\bar{p})$ from material balance, before the normalized time can be calculated. However, they claim that generally, 2 or 3 iterations are enough to find a converging solution for pseudo-time. The authors argue that the normalized time transformation does not affect the transient solutions, but that its main benefit is to improve forecast in boundary dominated flow. The explanation is that the average reservoir pressure does not decline significantly during transient flow. However, their results show that the analytical solutions for transient flow are dependent on the

comparison between the pressure drawdown and the initial pressure. In the modified model presented in this thesis, this drawdown dependence is taken into account by including the drawdown correction factor proposed by Ibrahim and Wattenbarger (2005) discussed in Chapter 2.

Anderson and Mattar (2005) showed that normalized time, which is based on average pressure, works well for boundary-dominated flow. However, they claim that this pseudo-time definition yields erroneous results if used during transient flow, especially for low permeability reservoirs. The explanation is that average reservoir pressure is a function of total pore volume; however, the boundaries have not been reached during transient flow, making average pressure a poor datum to use. The authors propose a correction to the pseudo-time definition by evaluating the product μC_t at the average pressure of the region of influence, rather than average reservoir pressure itself. However, calculating the region of influence introduces additional uncertainty to the model. Nobakht and Clarkson (2011) showed that there is a possibility that the distance of investigation is underestimated by the equation used, which causes the average pressure in the region of interest to be underestimated as well. An additional drawback is that if this definition of pseudo-time is used, the final equation for total fracture surface area requires an input of permeability, total compressibility and gas viscosity at initial reservoir pressure. By using the definition of pseudo-time shown in Eq. 5.3., the total fracture surface calculation does not require the input of these parameters and thus, eliminates additional uncertainty.

5.2 Development of Analysis Equations

In this thesis, Wattenbarger's model is being re-visited to include a dynamic formation permeability. The first step is to re-derive the original diffusivity equation that models linear flow. Using the definitions of pseudo-pressure and pseudo-time discussed in the previous section, the linearized form of the diffusivity PDE for linear flow with dynamic permeability is presented in **Eq. 5.7**. The detailed derivation is shown in **Appendix B.1**.

$$\frac{\partial^2 m_k(p)}{\partial x^2} = \frac{\phi_i}{0.00633}\frac{\partial m_k(p)}{\partial t_{ap}} \tag{5.7a}$$

$$t_a(p) \approx \sum_{j=1}^{n} \frac{\Delta t_j}{(\mu C_t)_j} \tag{5.7b}$$

The following equations (**Eq. 5.8 - Eq. 5.10**) represent the dimensionless groups that can be derived from the PDE. The detailed derivation is shown in **Appendix B.2**.

$$\frac{1}{q_D} = \frac{x_f h\left[m_k(p_i) - m_k(p_{wf})\right]}{2236 q_g LT} \tag{5.8}$$

$$x_D = \frac{x}{L} \tag{5.9}$$

$$t_D = \frac{0.00633}{\phi_i L^2} t_{ap} \tag{5.10}$$

Similar to Wattenbarger's method, the derivation of the total fracture surface area starts from the "short term" approximation for constant pressure inner boundary shown in **Eq. 5.11**, which accounts for the transient part of the solution.

$$\frac{1}{q_D} = \sqrt{\pi t_D} \tag{5.11}$$

Substituting the new definitions for dimensionless gas rate and time, and manipulating the equation to be of the form y=mx, the resulting equation becomes **Eq. 5.12**. This equation is the basis of the $\sqrt{t}$ plot, and the slope value is defined analytically by **Eq. 5.13** with units of $m_{k_{cp}}$: $1/D^{\frac{1}{2}}/Mscf$.

$$k_m = k_0 \left[1 - \left(\frac{P_c - \alpha p}{P_1}\right)^m\right]^3 \tag{5.12}$$

$$m_{k_{cp}} = \frac{315.3\,T}{x_f h \sqrt{\phi_i}} \frac{1}{\Delta m_k(p)} \tag{5.13}$$

The m_{cp} equation can be solved for x_f, and substituting the resulting x_f equation in the well fracture surface area definition shown in Eq. 3.12, the fracture surface area equation becomes **Eq. 5.14**. The drawdown correction factor is included in the equation since the well has a fixed bottom-hole pressure, and is produced at a high drawdown. The detailed derivation of the model is shown in **Appendix B.3**.

$$A = f_{cp} \times \frac{1261.2\,T}{m_{k_{cp}} \sqrt{\phi_i}} \times \frac{1}{\Delta m_k(p)} \times n \tag{5.14}$$

It is important to highlight the strengths of this equation. First of all, in general, the surface area calculation is independent of time, which means that engineers can perform this analysis early in the life of the well to evaluate the effectiveness of the hydraulic fracturing job. This is the reason why the simulation model was run only for one year, since it is important to determine the productivity of the fractures early in the life of the well. Another benefit is that uncertain parameters such as gas viscosity, total compressibility and fracture half-length are not an input in the surface area equation; thus,

these uncertainties do not hinder the accuracy of the total fracture surface area calculation. If a different definition of pseudo-time had been used, average and initial values of gas viscosity and total compressibility would have been required to perform the analysis, and thus, additional uncertainties would have been introduced in the model. In this case, using the correction factor is enough to correct for any uncertainties in the analytical model.

As a summary of this discussion, **Table 19** shows a comparison of the equations used in Wattenbarger's model and their modified version when including dynamic matrix permeability.

Table 19 - Main Equations Used in RTA for Original and Modified Methods

	Wattenbarger (1998)	**Modified by Pelaez (2016)**
$\frac{1}{q_D}$	$\frac{kh\left[m(p_i)-m(p_{wf})\right]}{1424\, q_g T}$	$\frac{x_f h\left[m_k(p_i)-m_k(p_{wf})\right]}{2236 q_g L T}$
t_D	$\frac{0.00633k}{(\phi\mu c_t)_i\, x_f^2}\, t$	$\frac{0.00633}{\phi_i L^2}\, t_{ap}$
$m(p)/m_k(p)$	$2\int_{p_0}^{p}\frac{p}{z\mu}dp$	$2\int_{P_b}^{P}\frac{k_g P}{z\mu}\, dp$
t/t_{ap}	$time$	$\int_0^t \frac{k_g}{\mu C_t}dt$
$m_{cp}/m_{k_{cp}}$	$\frac{315.4T}{x_f h\sqrt{(\phi\mu c_t)_i}}\frac{1}{\Delta m(p)\sqrt{k}}$	$\frac{315.4\, T}{x_f h\sqrt{\phi_i}}\frac{1}{\Delta m_k(p)}$
A	$f_{cp}\frac{1261.2\, T}{\sqrt{(\phi\mu C_t)_i}}\times\frac{1}{\sqrt{k}\, m_{cp}\Delta m(p)}\times n$	$f_{cp}\times\frac{1261.2\, T}{\sqrt{\phi_i}}\times\frac{1}{m_{k_{cp}}\Delta m_k(p)}\times n$

5.3 Validation of the Model

The validity of the dynamic permeability analytical model was demonstrated by comparing the results from the simulation model to the analytic solution for transient linear flow. As explained in section 3.3, the first step is to convert the simulation results into dimensionless rate. However, in this case, the equation that should be used for dimensionless rate is Eq. 5.8. Also, the analytical solution has to be corrected for high drawdown by using Ibrahim and Wattenbarger's correction factor (f_{cp}) as shown in **Eq. 5.15**.

$$\frac{1}{q_D} = f_{cp}\sqrt{\pi t_D} \tag{5.15}$$

The same synthetic data that was used in the simulation with constant permeability shown in Table 1 was used in this model. However, there was a dynamic permeability introduced in the simulation model as shown in **Table 20**. **Fig. 27** shows the comparison between both methods; the results agree with each other very well since the two cases overlay each other from a very early time $t_D = 1e^{-4}$.

Table 20 - Dynamic Reservoir Data Used in Forward Simulation

Pressure	*Z-factor*	*Viscosity (cp)*	*k gas (md)*
0	1	0.013207742	2.78022E-06
500	0.963733915	0.013669201	2.57847E-05
700	0.950860317	0.013941863	1.76362E-05
900	0.939122689	0.014253261	1.34611E-05
1000	0.933722206	0.014422801	1.20952E-05
1100	0.928655711	0.01460129	1.10269E-05
1300	0.919585331	0.01498432	9.49159E-06
1500	0.912021194	0.015400666	8.47185E-06
1700	0.906049181	0.015848335	7.77042E-06
1900	0.90172527	0.016324923	7.27673E-06
2100	0.89907184	0.016827618	6.92475E-06
2300	0.898077125	0.017353283	6.6731E-06
2500	0.898697843	0.017898574	6.4948E-06
2700	0.900864355	0.018460085	6.37174E-06
2900	0.904487312	0.01903448	6.29137E-06
3100	0.909464623	0.019618594	6.24482E-06
3500	0.92304755	0.020804631	6.22914E-06
3800	0.935986056	0.021700204	6.26923E-06

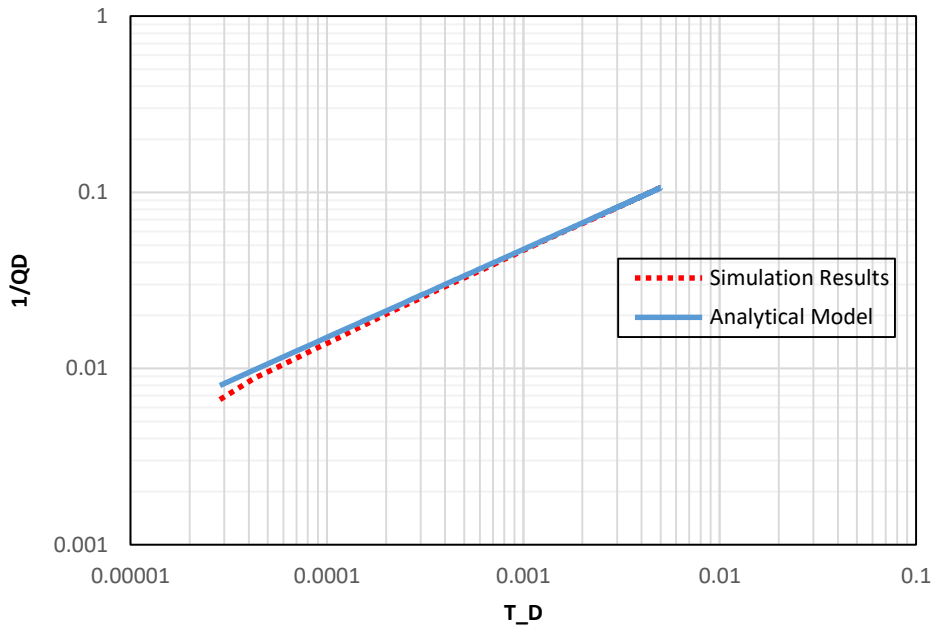

Figure 27 - Verification of the Analytical Model Developed for Dynamic Permeability

The next step is to verify if the correct value of total fracture surface area from the simulation model can be retrieved with the modified analytical equation derived in the previous section. However, since the derivation includes pseudo-time, the procedure to analyze the results and plot the $\sqrt{t_{ap}}$ plot becomes more complex. Thus, below there is an outline of the procedure that must be followed to be able to get the correct slope from the $\sqrt{t_{ap}}$ plot.

Procedure:

1. Export from the simulator the gas rate/day results and the average pressure curve. Thus, three columns must be available, time, gas rate-daily and average reservoir pressure.
2. Make a log-log plot of q_g vs time plot to identify formation linear flow by a negative-half slope as shown in **Fig. 28**.
3. Tabulate pressure dependent data (from smallest to largest), and calculate the following: z-factor, viscosity (μ), gas formation volume factor (B_g), gas compressibility (C_g), formation permeability (k_{gas}), real gas pseudo-pressure ($m(p)_k$), and the pseudo-time integrand ($\frac{k_g}{\mu C_t}$).
4. Arrange the pressure data back to the original sequence (highest to lowest). In order to calculate pseudo-time (t_{ap}), integrate the pseudo-time integrand ($\frac{k_g}{\mu C_t}$) with respect to time. The integration can be done using trapezoidal rule using **Eq. 5.16**.

$$t_{ap} = \sum_{i=1}^{N} \frac{(t_i - t_{i-1})}{2} \times \left[\left(\frac{k_g}{\mu C_t} \right)_i + \left(\frac{k_g}{\mu C_t} \right)_{i-1} \right] \tag{5.16}$$

5. Plot $\frac{1}{q_g} vs \sqrt{t_{ap}}$ in Cartesian coordinates and fit a linear trend line to read the value of the slope (m_{cp}). This plot is shown in **Fig. 29** and the value of $m_{cp} = 0.00082$ 1/D$^{1/2}$/MSCF.

Following the procedure described above, it is possible to obtain a value for m_{cp} and use it to calculate surface area. **Table 21** shows the value of total fracture surface area from both methods and the results differ by 0.18%. Thus, the validity of the model is demonstrated. This shows that the error caused by using a constant permeability assumption can be eliminated by applying this modified method instead.

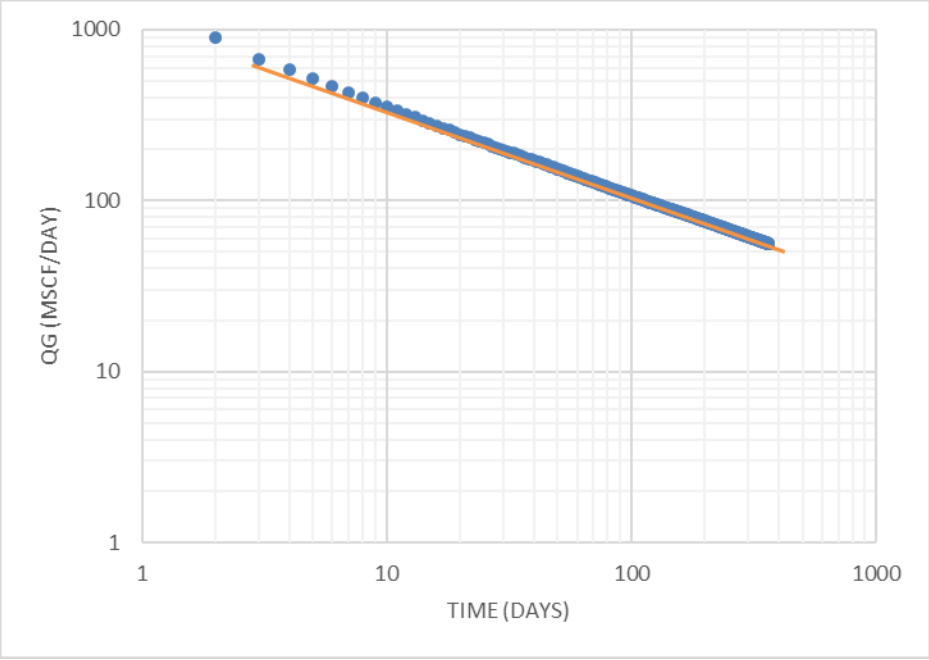

Figure 28 - Log-Log Plot Showing Matrix Transient Linear Flow

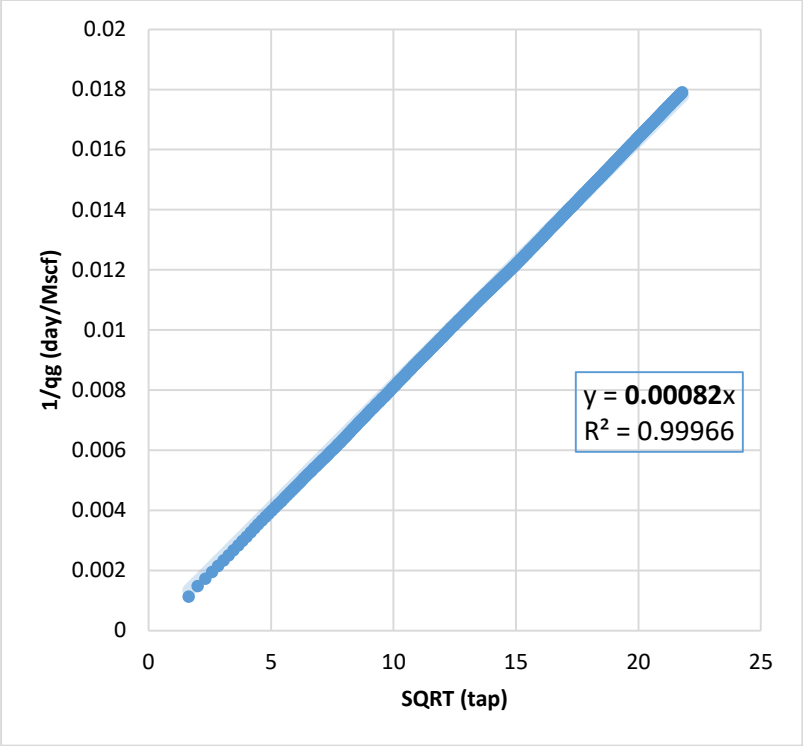

Figure 29 - SQRT Pseudo-Time Plot Yields an Accurate Slope to Use in the Analytical Model

Table 21 - Total Fracture Surface Area Modified for Dynamic Constant Permeability Comparison between Analytic and Simulation Models

Surface Area Calculation		
Simulation Model		
$A = 4 \times h \times x_f \times n$	2,075,000 47.64	*ft2* *acres*
Analytical Model		
$A = f_{cp} \times \frac{1261.2 \times T}{m_{cp}\sqrt{\phi_i}} \times \frac{1}{\Delta m_k(p)} \times n$	2,071,353 47.55	*ft2* *acres*
Error	0.18	*%*

CHAPTER VI

CONCLUSIONS

6.1 Conclusions

The major conclusions from this work can be summarized as follows:

1. Using a constant permeability value obtained from a permeability measurement without effective stress in the analysis of formation linear flow, results in a 79% error in the calculation of total fracture surface area. Thus, a permeability value measured without the presence of effective stress should not be used in a reservoir model.

2. Adjusting the measured permeability value for effective stress at reservoir conditions decreases the error in SA calculation significantly. Using Gangi's model as the dynamic permeability model, the error is reduced from 86.5% to 15.0%. Using the organic-rich apparent permeability model (Wasaki and Akkutlu, 2015), the error is reduced from 79% to 32%.

3. There is a range of 8% - 28% error in the calculated total fracture surface area caused by the assumption of constant permeability in the analytical model when using Gangi's model as the dynamic permeability model in the simulation. The error in surface area decreases as the initial permeability of the formation increases.

4. The range of error of fracture surface area is increased dramatically (1% - 323%) when using the apparent permeability model due to the permeability enhancement near the fractures from molecular transport mechanisms.

5. The total fracture surface area calculation is most sensitive to the geomechanic (stress-sensitive) parameters (P_c, p_1 and m). The next most important category is the sorption parameters including Langmuir volume (V_{sL}) and organic content (ε_{ks}).

6. Transient linear flow theory has been re-visited, and a modified analytical model to calculate the total fracture surface area which accounts for dynamic formation permeability is presented in this thesis. The error in total fracture surface area caused by assuming constant permeability is corrected when using the modified analytical model accounting for a dynamic permeability.

7. The benefits of the modified model include: a) Uncertain parameters such as permeability, fracture half-length, initial formation compressibility and initial gas viscosity are not an input in the area equations, thus, these uncertainties don't hinder the accuracy of the drainage and surface area calculations. b) The surface area calculation is independent of time; thus, as long as the well is already exhibiting formation linear flow, an accurate value for surface area can be calculated early in the life of the well to evaluate the effectiveness of the hydraulic fracturing job.

6.2 Recommendations for Future Work

1. The total fracture surface area calculation including dynamic permeability should be tested with production data from the field.

2. Shale reservoirs are not homogeneous; they have a dual porosity composed of matrix and fractures, which can be naturally or hydraulically created. Thus, the dual porosity analytical solutions for transient linear flow should be re-visited to account for dynamic matrix permeability.

3. Permeability is a tensorial quantity; however, in this study it has been treated as an isotropic quantity. Thus, an investigation on the effects of anisotropy on total fracture surface calculation is recommended for further study.

REFERENCES

Agarwal, R.G. 1979. Real gas Pseudo-time – A New Function for Pressure Buildup Analysis of MHF Gas Wells. Paper SPE 8279 presented in the 54th SPE Annual Fall Technical Conference and Exhibition held in Las Vegas, Nevada, September 23-36.

Ahmadi, H.A., Almarzooq, A.M. and Wattenbarger, R.A. 2010. Application of Linear Flow Analysis to Shale Gas Wells-Field Cases. Paper SPE 130370 presented at the Unconventional Gas Conference held in Pittsburgh, Pennsylvania, USA, 23-35 February.

Ambrose, R.J., Hartman, R.C., Diaz-Campos, M., Akkutlu, I.Y., and Sondergeld, C.H. 2012. Shale Gas in-place Calculations Part I - New Pore-scale Considerations. *SPE Journal*, Volume 17 (1) 219-229.

Anderson, D.M., and Mattar, L. 2007. An Improved Pseudo-time for Gas Reservoirs with Significant Transient Flow. *Journal of Canadian Petroleum Technology*, Volume 46 (7) 49-54.

Anderson, D.M., Nobakht, M., Moghadam, S., and Mattar, L. 2010. Analysis of Production Data from Fractured Shale Gas Wells. 2010. SPE Unconventional Gas Conference, 23-25 February, Pittsburgh, Pennsylvania.

Arevalo Villagran, J.A., Wattenbarger, R.A., Samaniego-Verduzco, F. and Pham, T.T. 2001. Production Analysis of Long-Term Linear Flow in Tight Gas Reservoirs: Case Histories. Paper SPE 71516 presented at the SPE Annual Technical Conference and Exhibition held in New Orleans, Louisiana, 30 September-3 October.

Bello, R.O. 2009. Rate Transient Analysis in Shale Gas Reservoirs with Transient Linear Behavior. PhD Dissertation, Texas A&M U., College Station, Texas.

Bello, R.O. and Wattenbarger, R.A. 2010. Multi-stage Hydraulically Fractured Shale Gas Rate Transient Analysis. Paper SPE 126754 presented at the SPE North Africa Technical Conference and Exhibition held in Cairo, Egypt, 14-17 February.

Carlson, E.S. and Mercer, J.C. 1989. Devonian Shale Gas Production: Mechanisms and Simple Models. *J Pet Tech* Volume 43 (4), 476-482.

El-Banbi, A.H. 1998. Analysis of Tight Gas Wells. PhD Dissertation, Texas A&M U., College Station, TX.

Fathi, E., and Akkutlu, I.Y. 2009. Matrix Heterogeneity Effects on Gas Transport and Adsorption in Coalbed and Shale Gas Reservoirs. *Journal of Transport in Porous Media*, Volume 80 (2), 281-304.

Fathi, E., Tinni A., and Akkutlu, I.Y. 2012. Correction to Kinkenberg Slip Theory for Gas Flow in Nano-capillaries. *International Journal of Coal Geology*, special issue on Shale, Volume 103, 51-59.

Fredd, C.N., McConnell, S.B., Boney, C.L., and England, K.W. 2001. Experimental Study of Fracture Conductivity for Water-Fracturing and Conventional Fracturing Applications. *SPE Journal*, Volume 6 (3), 288-298.

Gangi, A.F. 1978. Variation of Whole and Fractured Porous Rock Permeability with Confining Pressure. *International Journal of Rock Mechanics and Mining Sciences and Geomechanics Abstracts*, Volume 15 (5) 249-257.

Heller, R., and Zoback, M. 2013. Laboratory Measurements of Matrix Permeability and Slippage Enhanced Permeability in Gas Shales. Unconventional Resources Technology Conference, 12-14 August, Denver, Colorado, USA.

Ibrahim, M. and Wattenbarger, R.A. 2005. Analysis of Rate Dependence in Transient Linear Flow in Tight Gas Wells. Paper CIPC 2005-057 presented at the Canadian International Petroleum Conference, 7-9 June, Calgary, Alberta, Canada.

Karniadakis, G., Beskok, A., and Aluru, N. 2005 *Microflows and Nanoflows: Fundamentals and Simulation*. Springer, New Yok.

Kucuk, F., and Sawyer, W.K. 1980. Transient Flow in Naturally Fractured Reservoirs and its Application to Devonian Gas Shales. 55th Annual Fall Technical Conference and Exhibition of the Society of Petroleum Engineers of AIME, 21-24 September, Dallas, Texas.

Kwon, O., Kronenberg, A.K., Gangi, A.F., Johnson, B., and Herbert, B.E. 2004. Permeability of Illite-bearing Shale: 1. Anisotropy and Effects of Clay Content and Loading. *Journal of Geophysical Research-Solid Earth*, Volume 109 (B10), B10205.

Liang, P., Mattar, L., and Moghadam, S. 2011. Analyzing Variable Rate/Pressure Data in Transient Linear Flow in Unconventional Gas Reservoirs. Canadian Unconventional Resources Conference, 15-17 November, Calgary, Alberta, Canada.

Mayerhofer, M.J., Lolon, E.P., Youngblood, J.E. and Heinze, J.R. 2006. Integration of Microseismic Fracture Mapping Results with Numerical Fracture Network Production Modeling in the Barnett Shale. SPE Annual Technical Conference and Exhibition, 24-27 September, San Antonio, Texas.

Nobakht, M., and Clarkson, C.R. 2011. A New Analytical Method for Analyzing Production Data from Shale Gas Reservoirs Exhibiting Linear Flow: Constant Pressure Production. Americas Unconventional Gas Conference, 14-16 June, The Woodlands, Texas.

Nobakht, M., Mattar, L., Moghadam, S., and Anderson, D.M. 2010. Simplified Yet Rigorous Forecasting of Tight/Shale Gas Production in Linear Flow. SPE Western Regional Meeting, 27-29 May, Anaheim, California.

Riewchotisakul, S. 2015. Effects of Adsorption on Molecular Transport in Nanotube. MSc Thesis, Texas A&M Univeristy, College Station, Texas (May 2015).

Vairogs, J., Hearn, C.L., Dareing, D.W., Rhoades, V.W., 1971. Effect of Rock Stress on Gas Production from Low-Permeability Reservoirs. *Journal of Petroleum Technology*, September.

Warren, J.E., and P.J. Root, 1963. The Behavior of Naturally Fractured Reservoirs. *SPE Journal, Trans., AIME*, 228, 245-255.

Wasaki, A. 2015. Dynamics of Matrix-Fracture Coupling During Shale Gas Production. MSc Thesis, Texas A&M Univeristy, College Station, Texas (May 2015).

Wasaki, A. and Akkutlu, I.Y. 2015. Permeability of Organic-rich Shale. *SPE Journal*, Volume 20 (6), 1384-1396.

Wasaki, A. and Akkutlu, I.Y. 2015. Dynamics of Fracture-matrix Coupling during Shale Gas Production: Pore Compressibility and Molecular Transport Effects. Paper SPE 175033 presented at the SPE Annual Technical Conference and Exhibition held in Houston, Texas, USA, 28-30 September.

Wattenbarger, R.A., El-Banbi, A.H., Villegas, M.E., and Maggard, J.B. Production Analysis of Linear Flow into Fractured Tight Gas Wells. Paper SPE 39931 presented at SPE Rocky Mountain Regional/Low Permeability Reservoirs Symposium and Exhibition held in Denver, Colorado, 5-8 April.

Wen, Q., Zhang, S., Wang, L., Liu, Y., and Li, X. 2007. The Effect of Proppant Embedment Upon Long-term Conductivity of Fractures. *Journal of Petroleum Science and Engineering*, Volume 55 (3-4), 221-227.

Xu, B., Haghighi, M., and Cooke, D. 2012. Production Data Analysis in Eagle Ford Shale Gas Reservoir. SPE/EAGE European Unconventional Resources Conference and Exhibition, 20-22 March, Vienna, Austria.

Zhang, J., Kamenov, A., Hill, A.D., and Zhu, D. 2014. Laboratory Measurement of Hydraulic-Fracture Conductivities in the Barnett Shale. *SPE Production & Operations*, Volume 29 (3), 216-227.

APPENDIX A

A.1. Derivation of Solution for Linear Flow into Fractured Wells – Constant Pressure Condition

In this section, the detailed derivation of the solution for linear flow into fractured wells (Eq. 3 in Wattenbarger et al.) is presented, since it was not found readily available in the literature. This material was developed with the contribution of J.B. Maggard.

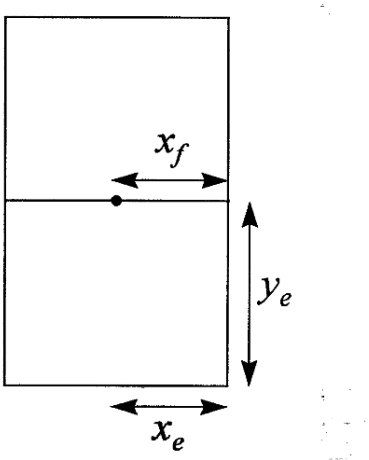

Figure 30 - A hydraulically fractured well in a rectangular reservoir from Wattenbarger et al. (1998)

The analytical model is based on the following assumptions:

- Infinite conductivity fracture extending all the way to drainage boundary (x_f=x_e)
- Solutions are for both infinite-acting and stabilized flow
- Eq. 3 is the solution for constant pressure left boundary condition and no flow (closed) right boundary condition

The partial differential equation (PDE) for linear flow is,

$$\frac{\partial^2 p_D}{\partial x^2} = \frac{\partial p_D}{\partial t}$$

where $p_{D_{xx}} = p_{D_t}\ for\ domain\ 0 \le x \le 1, t > 0$

A commonly used definition of p_D is,

$$p_D = \frac{p_i - p(x,t)}{p_i - p_{wf}}$$

The initial (I.C.) and boundary conditions (B.C.) are defined as follows,

$$\text{I.C.} \quad p_D[x,0] = 0$$

$$\text{B.C.} \quad p_D[0,t] = 1$$

$$p_{D_x}[1,t] = 0$$

The Fourier series solution has the form,

$$p_D[x,t] = v[x,t] + w[x,t]$$

where the first term is the steady (SS) portion of the solution and the second term is the transient portion.

In this case, the SS portion is,

$$v[x] = 1$$

which satisfies the PDE and both boundary conditions.

In order to satisfy the initial condition, the following relationship must be true,

$$w[x,0] = -v[x]$$

As time moves forward, the general solution moves from the initial condition to the SS condition, while always satisfying the PDE and both boundary conditions.

The transient part of the solution: $w[x,t]$ must also satisfy the PDE and must not modify the B.C. already satisfied by v[x]. Thus,

$$w[0,t] = 0 \text{ and } w_x[1,t] = 0$$

The Fourier Series (only odd numbered term) was obtained through Mathematica for the negative of $v[x] = 1$, with Fourier parameters {0→ π/2}. The nth term of the series is,

$$w(x) = -v(x) = \frac{-4}{\pi} \sum_{n=1\ odd}^{\infty} \frac{\sin\left[\frac{n\pi x}{2}\right]}{n}$$

Including exponential decay to satisfy the PDE as the solution moves from initial conditions to SS,

$$w_{nth}[x,t] = -\frac{4}{n\pi}\sin\left[\frac{n\pi x}{2}\right] e^{-\frac{tn^2\pi^2}{4}}$$

When differentiating with respect to time and twice with respect to x,

$$w_{xx} = w_t = -e^{-\frac{1}{4}n^2\pi^2 t}\, n\pi \sin\left[\frac{n\pi x}{2}\right]$$

Thus, the transient portion also satisfies the PDE over the domain (0≤x≤1, t>0).

Differentiating with respect to x for x=1,

$$w_x = 2e^{-\frac{1}{4}n^2\pi^2 t}\, \cos\left[\frac{n\pi x}{2}\right]$$

Since n is always odd; when x=1, every term becomes zero, which satisfies $w_x[1,t] = 0$.

Thus, the full Fourier Solution to Transient/BDF becomes

$$p_D[x,t] = 1 + \left(-\frac{4}{\pi}\right) \sum_{n=1\ odd}^{\infty} \frac{sin\left[\frac{n\pi x}{2}\right] e^{-\frac{tn^2\pi^2}{4}}}{n}$$

Since the dimensionless flow rate is defined as:

$$q_D = -p'_D[0,t]$$

Then,

$$q_D = 2\sum_{n=1\ odd}^{\infty} e^{-tn^2\frac{\pi^2}{4}}$$

The inverse of the dimensionless flow rate is:

$$\frac{1}{q_D} = \frac{1}{2\sum_{n=1\ odd}^{\infty} e^{-tn^2\frac{\pi^2}{4}}}$$

In order to match Eq. 3 in SPE 39931 it's necessary to define *t*:

$$t = t_{Dye} \text{ and } t_{Dye} = t_{Dxf}\frac{x_f^2}{y_e^2}$$

Thus, in terms of t_{Dxf}, the inverse of dimensionless rate is:

$$\frac{1}{q_D} = \frac{1}{2\sum_{n=1\ odd}^{\infty} e^{-n^2\frac{\pi^2}{4}\left(\frac{x_f^2}{y_e^2}\right)t_{Dxf}}}$$

A.2. Derivation of "Short-term" Approximation

This approximation is the solution for 1D linear flow infinite acting reservoir with constant pressure boundary condition.

Starting with 1D linear flow PDE (also presented in A1.1),

$$\frac{\partial^2 p_D}{\partial x^2} = \frac{\partial p_D}{\partial t}$$

The solution is $p(x,t)$ over domain $0 \le x \le \infty, t > 0$

I.C. $\quad p_D[x,0] = 0$

B.C. $\quad p_D[0,t] = 1$

$$\text{For } t > 0,\ p_D[\infty, t] = 0$$

Defining the Boltzmann transformation variable, s

$$s = \frac{x}{\sqrt{4t}}$$

Noting that,

$$\frac{ds}{dx} = \frac{1}{\sqrt{4t}} \ \therefore \frac{d}{dx} = \frac{1}{\sqrt{4t}}\frac{d}{ds}$$

$$\frac{ds}{dt} = \left(\frac{x}{\sqrt{4}}\right)\left(-\frac{1}{2}\right)t^{-\frac{3}{2}} = \left(\frac{x}{\sqrt{4t}}\right)\left(-\frac{1}{2t}\right) = -\frac{s}{2t}$$

Applying chain rule to the PDE,

$$\frac{\partial}{\partial x}\left(\frac{\partial p_D}{\partial s}\frac{\partial s}{\partial x}\right) = \frac{\partial p_D}{\partial s}\frac{\partial s}{\partial t}$$

Substituting derivatives into the PDE results in a second order ODE,

$$LHS:\ \frac{1}{\sqrt{4t}}\frac{d}{ds}\left(\frac{dp_D}{ds}\frac{1}{\sqrt{4t}}\right) = \frac{1}{4t}\frac{d^2p_D}{ds^2}$$

Thus, ODE becomes,

$$\frac{1}{4t}\frac{d^2p_D}{ds^2} = -\frac{s}{2t}\frac{dp_D}{ds}$$

Further simplifying,

$$\frac{d^2p_D}{ds^2} = -2s\frac{dp_D}{ds}$$

Now, the solution is $p_D(s)$, over domain $0 \leq s \leq \infty$ with boundary conditions as shown,

I.C. $\quad p_D(\infty) = 0$

B.C. $\quad$ For t>0, $p_D(0) = 1$

For t>0, $p_D(\infty) = 0$

Note that the three initial/boundary conditions for PDE have become only two conditions for ODE.

Let

$$p'_D = \frac{dp_D}{ds}$$

Substituting into ODE,

$$\frac{dp'_D}{ds} = -2s\, p'_D$$

Separating variables,

$$\frac{dp'_D}{p'_D} = -2sds$$

Integrating,

$$\ln(p'_D) = -s^2 + C_1$$

Inverting the natural logarithm,

$$p'_D = \frac{dp_D}{ds} = C_2 e^{-s^2} \; where \; C_2 = e^{C_1}$$

Separating and integrating, and considering the initial=right boundary condition as the lower limit of integration,

$$\int_{p(\infty)=0}^{p(s)} d\varphi = p_D(s) = C_2 \int_{\frac{x}{\sqrt{4t}}=\infty}^{\frac{x}{\sqrt{4t}}} e^{-s^2} ds$$

Recalling that,

$$erfc(s) = \frac{2}{\sqrt{\pi}} \int_s^{\infty} e^{-s^2} ds$$

Then, substituting erfc(s),

$$p_D(s) = C_2\left(-\frac{\sqrt{\pi}}{2}\ erfc(s)\right)$$

Since p_D (0) =1 at the left boundary, and recalling that erfc(0)=1,

$$C_2 = -\frac{2}{\sqrt{\pi}}$$

Finally,

$$p_D(x,t) = erfc\left(\frac{x}{\sqrt{4t}}\right)$$

Thus,

$$\frac{\partial p_D}{\partial x} = \frac{\partial}{\partial x}\left(erfc\left(\frac{x}{\sqrt{4t}}\right)\right) = -\frac{2}{\sqrt{4\pi t}} * e^{-\frac{x^2}{4t}} = \frac{-1}{\sqrt{\pi t}} * e^{-\frac{x^2}{4t}}$$

At the left boundary,

$$\frac{\partial p_D}{\partial x}\ at\ (0,t) = -\frac{1}{\sqrt{\pi t}}$$

"Long term" Approximation

This approximation is made by keeping only the first term of the series in the full solution.

Recalling that $q_D = -p_D'$

$$\frac{1}{q_D} = \frac{1}{2\sum_{n=1\ odd}^{\infty} e^{-tn^2\frac{\pi^2}{4}}}$$

Taking only the first term of the series,

$$\frac{1}{q_D} = \frac{1}{2}e^{t\frac{\pi^2}{4}}$$

A.3. Matching Derived Solutions with Wattenbarger et al. (SPE 39931)

From RAW Ch. 1,

$$p_D = 0.00633\ kA\frac{p_i - p}{qB\mu L}$$

Noting that $\frac{1}{141.2} = \frac{0.00633*2\pi}{5.615}$

$$A = 4hx_f \quad ; \quad L = y_e$$

$$p_D = \frac{5.615}{141.2 * 2\pi}\ k(4hx_f)\frac{p_i - p}{qB\mu y_e}$$

Simplifying and re-arranging,

$$p_D = \frac{5.615 * 2x_f}{y_e\pi}\ \frac{kh\ (p_i - p)}{141.2\ qB\mu}$$

From SPE paper Eq. 4,

$$p_{wD} = \frac{kh\ (p_i - p)}{141.2\ qB\mu}$$

Then,

$$p_D = \frac{\pi}{2}\left(\frac{y_e}{x_f}\right)\frac{1}{5.615}\ p_{wD}$$

Also noting that

$$t_D = t_{Dye} = \frac{0.00633kt}{\phi\mu c_t y_e^2} = t_{Dxf}\frac{x_f^2}{y_e^2}\ from\ SPE\ Eq.15$$

Thus, recalling "short term" approximation solution,

$$\frac{\partial p_D}{\partial x}\ at\ (0,t) = -\frac{1}{\sqrt{\pi t}}$$

Substituting t_{Dye} with t_{Dxf},

$$\frac{1}{q_D} = \sqrt{\pi t_{Dye}} = \sqrt{\pi t_{Dxf} \frac{x_f^2}{y_e^2}}$$

From conversion factor between p_D and p_{wD},

$$\frac{1}{q_D} = \left(\frac{\pi}{2}\frac{y_e}{x_f}\right)\sqrt{\pi t_{Dxf} \frac{x_f^2}{y_e^2}}$$

And finally,

$$\boldsymbol{\frac{1}{q_D} = \frac{\pi}{2}\sqrt{\pi t_{Dxf}} \ldots Eq\ 8\ from\ SPE\ paper}$$

Now, recalling full solution

$$\frac{1}{q_D} = \frac{1}{2\sum_{n=1\ odd}^{\infty} e^{-t_{Dye} n^2 \frac{\pi^2}{4}}}$$

Substituting t_{Dye} definition and adding conversion factor,

$$\frac{1}{q_D} = \left(\frac{\pi}{2}\frac{y_e}{x_f}\right)\frac{1}{2\sum_{n=1\ odd}^{\infty} e^{-t_{Dxf}\left(\frac{x_f^2}{y_e^2}\right) n^2 \frac{\pi^2}{4}}}$$

$$\boldsymbol{\frac{1}{q_D} = \frac{\left(\frac{\pi}{4}\frac{y_e}{x_f}\right)}{\sum_{n=1\ odd}^{\infty} e^{-n^2\frac{\pi^2}{4}\left(\frac{x_f^2}{y_e^2}\right) t_{Dxf}}} \ldots Eq.3\ from\ SPE\ paper}$$

Finally, in order to get the "long-term" approximation, only the first term of the series is used,

$$\frac{1}{q_D} = \left(\frac{\pi}{4}\frac{y_e}{x_f}\right) e^{\frac{\pi^2}{4}\left(\frac{x_f^2}{y_e^2}\right)t_{Dxf}} \quad \ldots \boldsymbol{Eq.\,10\ from\ SPE\ paper}$$

The type curve solution becomes,

$$\left(\frac{x_f}{y_e}\right)\frac{1}{q_D} = \frac{\left(\frac{\pi}{4}\right)}{e^{-n^2\frac{\pi^2}{4}t_{Dye}}} \quad \ldots \boldsymbol{Eq.\,14\ from\ SPE\ paper}$$

A.4. Application to Gas Wells

For gas wells, p_{wD} is replaced by m_{wD}

$$m_{wD} = \frac{1}{q_D} = \frac{kh\left[m(p_i) - m\left(p_{wf}\right)\right]}{1424\ q_g T}$$

where $m(p)$ is the real gas pseudo-pressure,

$$m(p) = 2\int_{p_0}^{p} \frac{p}{z\mu}\,dp$$

and

$$t_{Dye} = \frac{0.00633kt}{(\phi\mu c_t)_i\ y_e^2}$$

Square-Root of Time Plot

The most critical plot for the RTA is the $\frac{1}{q_g}$ vs. $\sqrt{t}$ plot, commonly referred to as the SQRT plot.

Starting from the "short-term" approximation for constant pressure,

$$\frac{1}{q_D} = \frac{\pi}{2}\sqrt{\pi t_{Dxf}}$$

And substituting

$$\frac{1}{q_D} = \frac{kh\left[m(p_i) - m\left(p_{wf}\right)\right]}{1424\, q_g T}$$

$$t_{Dxf} = \frac{0.00633kt}{(\phi\mu c_t)_i\, x_f^2}$$

The equation becomes,

$$\frac{kh\left[m(p_i) - m\left(p_{wf}\right)\right]}{1424\, q_g T} = \frac{\pi}{2}\sqrt{\pi}\sqrt{\frac{0.00633kt}{(\phi\mu c_t)_i\, x_f^2}}$$

Simplifying and rearranging,

$$\frac{1}{q_g} = \frac{315.4T}{h\sqrt{(\phi\mu c_t)_i}}\frac{1}{\Delta m(p)\sqrt{k}\, x_f}\sqrt{t}$$

The slope is defined as,

$$m_{cp} = \frac{315.4T}{h\sqrt{(\phi\mu c_t)_i}}\,\frac{1}{\Delta m(p)\sqrt{k}\, x_f}$$

Solving the m_{cp} equation for x_f,

$$x_f = \frac{315.4T}{h\sqrt{(\phi\mu c_t)_i}}\,\frac{1}{\Delta m(p)\sqrt{k}\, m_{cp}}$$

Calculation of Total Fracture Surface Area

From Fig. A1, the total fracture surface area is given by

$$A = 4hx_f n$$

where n is the number of fractures, h is the thickness of the formation in ft., and x_f is the fracture half-length.

Substituting x_f into total facture surface area equation,

$$A = \frac{1261.2 \times T}{\sqrt{(\phi\mu C_t)_i}} \times \frac{1}{m_{cp} \times \sqrt{k} \times \Delta m(p)} \times n$$

Multiplying by the correction factor accounting for drawdown,

$$D_D = \frac{\left[m(p_i) - m\left(p_{wf}\right)\right]}{m(p_i)}$$

$$f_{cp} = 1 - 0.0852 D_D - 0.0857 D_D^2$$

The final form of the total fracture surface area equation becomes,

$$A = f_{cp} \frac{1261.2 \times T}{\sqrt{(\phi\mu C_t)_i}} \times \frac{1}{m_{cp} \times \sqrt{k} \times \Delta m(p)} \times n$$

APPENDIX B

B.1 Derivation of the Linear Flow PDE with Dynamic Permeability

In this section, the diffusivity equation will be derived using a dynamic permeability pseudo-pressure. The diffusivity equation is derived by combining three equations: the continuity equation, an equation of motion and an equation of state (EOS). The continuity equation is,

$$-\frac{\partial(\rho u_x)}{\partial x} = \frac{\partial(\phi\rho)}{\partial t} \tag{B.1}$$

where ρ is in lbm/ft^3, u in STB/day-ft^2, x in ft and t in days.

From Darcy's Law (Equation of motion),

$$u_x = -0.00633\frac{k_x}{\mu}\frac{\partial p}{\partial x} \tag{B.2}$$

where k is in md, μ in cp, p in psia, x in ft, and u in rcf/day-ft^2.

Substituting Eq. 2 into Eq. 1,

$$\frac{\partial}{\partial x}\left(\rho\frac{k_x}{\mu}\frac{\partial p}{\partial x}\right) = \frac{1}{0.00633}\frac{\partial(\phi\rho)}{\partial t} \tag{B.3}$$

where ρ is in lbm/ft^3, k is in md, μ in cp, x in ft, p in psia and t in days.

From the real gas law (EOS),

$$\rho = \frac{M}{RT}\frac{p}{z} \tag{B.4}$$

Substituting Eq. 4 in Eq. 3,

$$\frac{\partial}{\partial x}\left(\frac{M}{RT}\frac{p}{z}\frac{k_x}{\mu}\frac{\partial p}{\partial x}\right) = \frac{\partial}{\partial t}\left(\phi\frac{M}{RT}\frac{p}{z}\right)$$

M, R, and T are constant, thus they are canceled out,

$$\frac{\partial}{\partial x}\left(\frac{p}{z}\frac{k_x}{\mu}\frac{\partial p}{\partial x}\right) = \frac{\partial}{\partial t}\left(\phi\frac{p}{z}\right) \tag{B.5}$$

Expanding the RHS of the equation,

$$\frac{\partial}{\partial t}\left(\phi\frac{p}{z}\right) = \phi\frac{\partial}{\partial t}\left(\frac{p}{z}\right) + \frac{p}{z}\frac{\partial\phi}{\partial t}$$

$$= \phi\frac{\partial}{\partial p}\left(\frac{p}{z}\right)\frac{\partial p}{\partial t} + \frac{p}{z}\frac{\partial\phi}{\partial p}\frac{\partial p}{\partial t}$$

$$= \phi\frac{p}{z}\left[\frac{z}{p}\frac{\partial}{\partial p}\left(\frac{p}{z}\right)\frac{\partial p}{\partial t} + \frac{1}{\phi}\frac{\partial\phi}{\partial p}\frac{\partial p}{\partial t}\right]$$

From compressibility, we know,

$$C_g = \frac{1}{\rho}\frac{\partial\rho}{\partial p} = \frac{z}{p}\frac{\partial}{\partial p}\left(\frac{p}{z}\right)$$

$$C_f = \frac{1}{\phi}\frac{\partial\phi}{\partial p}$$

$$C_t = C_g + C_f$$

Thus,

$$RHS = \phi C_t\frac{p}{z}\frac{\partial p}{\partial t}$$

And plugging the RHS in Eq. 5,

$$\frac{\partial}{\partial x}\left(\frac{p}{z}\frac{k_x}{\mu}\frac{\partial p}{\partial x}\right) = \phi C_t\frac{p}{z}\frac{\partial p}{\partial t} \tag{B.6}$$

Introducing pseudo-pressure modified for pressure dependent k_x ,

$$m_k(p) = 2\int_{p_0}^{p}\frac{k_x p}{z\mu}dp \tag{B.7}$$

where the partial derivatives are,

$$\frac{\partial m_k(p)}{\partial x} = \frac{\partial m_k(p)}{\partial p}\frac{\partial p}{\partial x} = 2\frac{k_x p}{z\mu}\frac{\partial p}{\partial x}$$

Thus,

$$\frac{\partial p}{\partial x} = \frac{z\mu}{2k_x p}\frac{\partial m_k(p)}{\partial x} \tag{B.8}$$

And,

$$\frac{\partial m_k(p)}{\partial t} = \frac{\partial m_k(p)}{\partial p}\frac{\partial p}{\partial t} = 2\frac{k_x p}{z\mu}\frac{\partial p}{\partial t}$$

$$\frac{\partial p}{\partial t} = \frac{z\mu}{2k_x p}\frac{\partial m_k(p)}{\partial t} \tag{B.9}$$

Thus, substituting Eq. 8 and 9 in Eq. 6,

$$\frac{\partial}{\partial x}\left(\frac{p}{z}\frac{k_x}{\mu}\frac{z\mu}{2k_x p}\frac{\partial m_k(p)}{\partial x}\right) = \phi C_t \frac{p}{z}\frac{z\mu}{2k_x p}\frac{\partial m_k(p)}{\partial t}$$

Canceling like terms,

$$\frac{\partial}{\partial x}\left(\frac{\partial m_k(p)}{\partial x}\right) = \frac{\phi C_t \mu}{k_x}\frac{\partial m_k(p)}{\partial t}$$

In field units,

$$\frac{\partial}{\partial x}\left(\frac{\partial m_k(p)}{\partial x}\right) = \frac{1}{0.00633}\frac{\phi C_t \mu}{k_x}\frac{\partial m_k(p)}{\partial t} \tag{B.10}$$

where *t* is in days.

Introducing Agarwal's pseudo-time modified for pressure dependent k_x,

$$t_{ap} = \int_0^t \frac{k_x}{\mu C_t}\,dt \tag{B.11}$$

The derivatives are,

$$\frac{\partial t_{ap}}{\partial t} = \frac{k_x}{\mu C_t}$$

$$\frac{\partial m_k(p)}{\partial t} = \frac{\partial m_k(p)}{\partial t_{ap}} \frac{\partial t_{ap}}{\partial t} = \frac{k_x}{\mu C_t} \frac{\partial m_k(p)}{\partial t_{ap}} \tag{B.12}$$

Substituting Eq. 12 in Eq. 10 to linearize the RHS,

$$\frac{\partial}{\partial x}\left(\frac{\partial m_k(p)}{\partial x}\right) = \frac{1}{0.00633} \frac{\phi C_t \mu}{k_x} \frac{k_x}{\mu C_t} \frac{\partial m_k(p)}{\partial t_{ap}}$$

Canceling like terms,

$$\frac{\partial}{\partial x}\left(\frac{\partial m_k(p)}{\partial x}\right) = \frac{\phi}{0.00633} \frac{\partial m_k(p)}{\partial t_{ap}}$$

Finally,

$$\frac{\partial^2 m_k(p)}{\partial x^2} = \frac{\phi}{0.00633} \frac{\partial m_k(p)}{\partial t_{ap}} \tag{B.13}$$

Note: The final equation is still not completely linear since porosity is a pressure dependent property based on the following equation.

$$c_f = \frac{1}{\phi} \frac{d\phi}{dp}$$

However, if the pressure range is small enough, porosity will not change too much.

B.2 Derivation of New Dimensionless Groups for 1-D Linear Flow

In this section, new dimensionless groups are derived for the diffusivity equation including dynamic permeability. Accounting for a dynamic permeability, the partial differential equation for 1-D linear flow is as derived in the previous section,

$$\frac{\partial^2 m_k(p)}{\partial x^2} = \frac{\phi}{0.00633}\frac{\partial m_k(p)}{\partial t_{ap}}$$

where

$$m_k(p) = 2\int_{p_0}^{p}\frac{kp}{z\mu}dp \quad and \quad t_{ap} = \int_0^t \frac{k}{\mu C_t}dt$$

Initial condition: $m_D(x_D, t_D = 0) = 0$

Constant rate Inner Boundary Condition: $\left[\frac{\partial m_D}{\partial x_D}\right]_{x_D=0} = -1$

Intuitive definition of x_D:

$$x_D = \frac{x}{L} \rightarrow \quad x = L\,x_D$$

Substituting the definition of x_D in the original PDE,

$$\frac{\partial^2 m_k(p)}{\partial (L\,x_D)^2} = \frac{\phi}{0.00633}\frac{\partial m_k(p)}{\partial t_{ap}}$$

$$\frac{1}{L^2}\frac{\partial^2 m_k(p)}{\partial {x_D}^2} = \frac{\phi}{0.00633}\frac{\partial m_k(p)}{\partial t_{ap}}$$

Multiplying through L^2

$$\frac{\partial^2 m_k(p)}{\partial {x_D}^2} = \frac{\phi L^2}{0.00633}\frac{\partial m_k(p)}{\partial t_{ap}}$$

$$y(x, \tau \le 0) = y_i \rightarrow m_D\left(x, t_{ap} \le 0\right) = 0$$

$$m_D = \frac{1}{m_k(p)_{ch}}(m_k(p_i) - m_k(p))$$

And rearranging to solve for $m_k(p)$,

$$m_k(p) = m_k(p_i) - m_k(p)_{ch} m_D$$

Substituting the definition of $m_k(p)_{ch}$ in the PDE,

$$\frac{\partial^2 (m_k(p_i) - m_k(p)_{ch}\, m_D)}{\partial {x_D}^2} = \frac{\phi L^2}{0.00633} \frac{\partial (m_k(p_i) - m_k(p)_{ch}\, m_D)}{\partial t_{ap}}$$

Expanding terms and eliminating constants,

$$\frac{\partial^2 \cancel{m_k(p_i)}}{\cancel{\partial x_D^2}} - m_k(p)_{ch} \frac{\partial^2 m_D}{\partial {x_D}^2} = \frac{\phi L^2}{0.00633} \left(\frac{\partial \cancel{m_k(p_i)}}{\cancel{\partial t_{ap}}} - m_k(p)_{ch} \frac{\partial m_D}{\partial t_{ap}} \right)$$

$$m_k(p)_{ch} \frac{\partial^2 m_D}{\partial {x_D}^2} = \frac{\phi L^2}{0.00633}\, m_k(p)_{ch} \frac{\partial m_D}{\partial t_{ap}}$$

Canceling $m(p)_{k_{ch}}$ in each term,

$$\frac{\partial^2 m_D}{\partial {x_D}^2} = \frac{\phi L^2}{0.00633} \frac{\partial m_D}{\partial t_{ap}}$$

Solving for the characteristic pressure:

Using Darcy's law,

$$u = -\frac{k}{\mu} \frac{\partial p}{\partial x}$$

Applying chain rule to the gradient,

$$u = -\frac{k}{\mu} \frac{\partial p}{\partial m_k(p)} \frac{\partial m_k(p)}{\partial x}$$

From the definition of velocity,

$$v = \frac{qB}{A} \rightarrow q = \frac{vA}{B}$$

Thus,

$$q = \frac{k}{\mu}\frac{A}{B}\frac{\partial p}{\partial m_k(p)}\frac{\partial m_k(p)}{\partial x}$$

where, A is the cross sectional area for flow, defined by

$$A = 4x_f h$$

Thus,

$$q = \frac{k}{\mu}\frac{4x_f h}{B}\frac{\partial p}{\partial m_k(p)}\left[\frac{\partial m_k(p)}{\partial x}\right]_{x=0}$$

Solving for the gradient,

$$\left[\frac{\partial m_k(p)}{\partial x}\right] = \frac{q\mu B}{4kx_f h}\frac{\partial m_k(p)}{\partial p}$$

For inner boundary condition (constant rate),

$$\left[\frac{\partial m_k(p)}{\partial x}\right]_{x=0} = \frac{q\mu B}{4kx_f h}\frac{\partial m_k(p)}{\partial p}$$

Substituting the definitions of x and $m(p)_k$ in the left hand side,

$$\left[\frac{\partial (m_k(p_i) - m_k(p)_{ch}\, m_D)}{\partial (L\, x_D)}\right]_{x_D=0} = \frac{q\mu B}{4kx_f h}\frac{\partial m_k(p)}{\partial p}$$

$$\left[\frac{1}{L}\frac{\partial m_k(p_i)}{\cancel{\partial x_D}} - \frac{m_k(p)_{ch}}{L}\frac{\partial m_D}{\partial x_D}\right]_{x_D=0} = \frac{q\mu B}{4kx_f h}\frac{\partial m_k(p)}{\partial p}$$

$$\left[\frac{\partial m_D}{\partial x_D}\right]_{x_D=0} = -\frac{q\mu BL}{4kx_f h}\frac{1}{m_k(p)_{ch}}\frac{\partial m_k(p)}{\partial p}$$

As a mathematical convenience we want,

$$\left[\frac{\partial m_D}{\partial x_D}\right]_{x_D=0} = -1$$

Equating both definitions,

$$-1 = -\frac{q\mu BL}{4kx_f h}\frac{1}{m_k(p)_{ch}}\frac{\partial m_k(p)}{\partial p}$$

Solving for the characteristic pressure,

$$m_k(p)_{ch} = \frac{q\mu BL}{4kx_f h}\frac{\partial m_k(p)}{\partial p}$$

Substituting this definition in the original p_D equation,

$$m_D = \frac{1}{m_k(p)_{ch}}(m_k(p_i) - m_k(p))$$

$$m_D = \frac{4kx_f h}{q\mu BL}\frac{1}{\left(\frac{\partial m_k(p)}{\partial p}\right)}(m_k(p_i) - m_k(p)) \qquad Darcy\ units\ system$$

Recalling the definition of $m_k(p)$,

$$m_k(p) = 2\int_{p_0}^{p}\frac{kp}{z\mu}dp$$

Then,

$$\frac{\partial m_k(p)}{\partial p} = 2\frac{kp}{z\mu}$$

Substituting this definition,

$$m_D = \frac{4kx_f h}{q\mu BL}\frac{z\mu}{2kp}(m_k(p_i) - m_k(p))$$

Canceling like terms,

$$m_D = \frac{2x_f h}{qBL}\frac{z}{p}(m_k(p_i) - m_k(p))$$

Using the definition for *B* for the following standard conditions:

$P_{sc} = 14.7psia\ and\ T_{sc} = 60°\text{F}$ with units of res. volume/ standard vol.,

$$B = 0.0283\frac{zT}{p}$$

$$m_D = \frac{2x_f h}{qL}\frac{z}{p}\frac{p}{0.0283\ zT}(m_k(p_i) - m_k(p))$$

Canceling like terms,

$$m_D = 70.67\frac{x_f h}{qLT}(m_k(p_i) - m_k(p))$$

Converting to field units,

$$m_D = \frac{1}{2236}\frac{x_f h}{q_g LT}(m_k(p_i) - m_k(p))$$

where q_g is in MSCF/day.

Recalling the intermediate solution,

$$\frac{\partial^2 m_D}{\partial x_D^2} = \left(\frac{\phi L^2}{0.00633}\right)\frac{\partial m_D}{\partial t_{ap}}$$

The term in the parentheses is the intuitive definition of t_D,

$$t_D = \frac{t_{ap}}{t_{apch}} \rightarrow\ t_{ap} = t_{apch}\ t_D$$

Substituting the definition of t_{ap} in the PDE,

$$\frac{\partial^2 m_D}{\partial x_D{}^2} = \frac{\phi L^2}{0.00633}\frac{1}{t_{apch}}\frac{\partial m_D}{\partial t_D}$$

$$t_{apch} = \frac{\phi L^2}{0.00633}$$

Finally,

$$\frac{\partial^2 m_D}{\partial {x_D}^2} = \frac{\partial m_D}{\partial t_D}$$

where

$$t_D = \frac{0.00633}{\phi L^2} t_{ap} \quad Field\ units$$

In summary, in field units, the dimensionless groups are,

$$m_D = \frac{1}{2236} \frac{x_f h}{q_g LT} (m_k(p_i) - m_k(p))$$

$$x_D = \frac{x}{L}$$

$$t_D = \frac{0.00633}{\phi L^2} t_{ap}$$

B.3 Derivation of the Total Fracture Surface Area Equation Using These Dimensionless Groups

Square-Root of Time Plot

Starting from the "short-term" approximation for constant pressure,

$$\left[\frac{\partial m_D}{\partial x_D}\right]_{x_D=0} = -\frac{1}{\sqrt{\pi t_D}}$$

$$\frac{1}{q_D} = \sqrt{\pi t_D}$$

And substituting the dimensionless groups,

$$\frac{1}{q_D} = \frac{1}{2236} \frac{x_f h}{q_g LT} (m_k(p_i) - m_k(p))$$

$$t_D = \frac{0.00633}{\phi L^2} t_{ap}$$

The equation becomes,

$$\frac{1}{2236} \frac{x_f h}{q_g LT} (m_k(p_i) - m_k(p)) = \sqrt{\pi \left(\frac{0.00633}{\phi L^2} \; t_{ap} \right)}$$

Simplifying and rearranging,

$$\frac{1}{q_g} = \frac{315.3\, T}{x_f h \sqrt{\phi_i}} \frac{1}{\Delta m_k(p)} \sqrt{t_{ap}}$$

The slope becomes,

$$m_{cp_k} = \frac{315.3\, T}{x_f h \sqrt{\phi_i}} \frac{1}{\Delta m_k(p)}$$

Solving for x_f,

$$x_f = \frac{315.3\, T}{h \sqrt{\phi_i}} \frac{1}{m_{k_{cp}} \Delta m_k(p)}$$

Calculation of Total Fracture Surface Area

From Fig. 3, the total fracture surface area is given by,

$$A = 4 h x_f n$$

Substituting equation for x_f into total fracture surface area equation and including the correction factor for drawdown, the final equation becomes,

$$A = f_{cp} \frac{1261.2 \; \times T}{\sqrt{(\phi \mu C_t)_i}} \times \frac{1}{m_{k_{cp}} \times \sqrt{k_g} \times \Delta m_k(p)} \times n$$